Spatio-temporal variations in surface Marine Carbonate System properties across the Western Mediterranean Sea using Volunteer Observing Ship data.

David Curbelo-Hernández*, David González-Santana, Aridane González-González, J. Magdalena Santana-Casiano and Melchor González-Dávila

[1] Instituto de Oceanografía y Cambio Global (IOCAG), Universidad de Las Palmas de Gran Canaria (ULPGC). Las Palmas de Gran Canaria, Spain.

* Corresponding Author: david.curbelo@ulpgc.es

Abstract

The surface physical and Marine Carbonate System (MCS) properties were assessed along the western boundary of the Mediterranean Sea. An unprecedented high-resolution observation-based dataset spanning 5 years (2019-2024) was built through automatically underway monitoring by a Volunteer Observing Ship (VOS). The MCS dynamics were strongly modulated by physical-biological coupling dependent on the upper-layer circulation and mesoscale features. The variations in CO_2 fugacity ($fCO_{2,sw}$) were mainly driven by sea surface temperature (SST) changes. On a seasonal scale, SST explained 45-83% of the increase in $fCO_{2,sw}$ from February to September, while total alkalinity (AT) and sea surface salinity (SSS) explained <15%. The processes controlling total inorganic carbon (C_T) partially offset this increment and explained ~25-38% of the $fCO_{2,sw}$ seasonal change. On an interannual scale, the SST trends (0.26-0.43 ºC yr^{-1}) have accelerated by 78-88% in comparison with previous decades. The ongoing surface warming contributed by ~76-92% in increasing $fCO_{2,sw}$ (4.18 to 5.53 µatm yr^{-1}) and, consequently, decreasing pH (-0.005 to -0.007 units yr^{-1}) in the surface waters. The seasonal amplitude of SST, becoming larger due to progressively warmer summers, was the primary driver of the observed slope up of interannual trends. The evaluation of the air-sea CO_2 exchange shows the area across the Alboran Sea (14,000 Km^2) and the eastern Iberian margin (40,000 Km^2) acting as an atmospheric CO_2 sink of -1.57 ± 0.49 mol m^{-2} yr^{-1} (0.97 ± 0.30 Tg CO_2 yr^{-1}) and -0.70 ± 0.54 mol m^{-2} yr^{-1} (-1.22 ± 0.95 Tg CO_2 yr^{-1}), respectively. Considering the spatial variability of CO_2 fluxes across the study area, a reduction of approximately 40–80% in the net annual CO_2 sink is estimated since 2019, which is attributed to the persistent strengthening of the source status during summer and the weakening of the sink status during spring and autumn.

Keywords: Marine Carbonate System, Air-sea CO_2 fluxes, Volunteer Observing Ships, Western Mediterranean Sea, ocean acidification, sea-surface warming

1. Introduction

The semi-enclosed and marginal seas have a relevant role in the global biogeochemical cycles and are highly vulnerable to climate change (IPCC, 2023). These regions accomplish extensive coastal and continental shelf and slope areas occupied with multiple diverse ecosystems under anthropogenic pressure. Although these regions present enhanced biogeochemical activity and intensified air-sea CO_2 exchange rates compared to the open ocean (Borges et al., 2005; Cai et al., 2006; Frankignoulle and Borges, 2001; Shadwick et al., 2010), its poorly monitoring and assessment have historically excluded them from global studies and models and underestimated in the Global Carbon Budget (Friedlingstein et al., 2023)

The Mediterranean Sea is a dynamic semi-enclosed system potentially fragile to natural and anthropogenic forcing (e. g. Álvarez et al., 2014; Tanhua et al., 2013). The particular oceanography of the Mediterranean Sea, collectively described in several works (e.g. Nielsen, 1912; Robinson et al., 2001; Millot and Taupier-Letage, 2005; Bergamasco and Malanotte-Rizzoli, 2010; Schroeder et al., 2012), have rendered it a "miniature ocean" considered as "laboratory basin" to evaluate physico-chemical perturbations that can be extrapolated to larger scales in the global ocean (e.g. Robinson and Golnaraghi, 1994; Bergamasco and Malanotte-Rizzoli, 2010). These perturbations have accelerated since the second half of the 20th century, with temperature and salinity increasing at unprecedent rates of 0.04ºC and 0.015 per decade, respectively (Borghini et al., 2014), impacting the Marine Carbonate System (MCS). However, the availability of high-quality observation-based data and research in this basin is scarce due to spatial and temporal limitations in the monitoring and sampling techniques (Millero et al., 1979; Rivaro et al., 2010).

The MCS dynamics has been evaluated in the Northwestern Mediterranean basin (Bégovic and Copin-Montégut, 2002; Copin-Montégut and Bégovic, 2002, 2004; Coppola et al., 2020; Hood and Merlivat, 2001; Mémery et al., 2002; Merlivat et al., 2018; Touratier and Goyet, 2009; Ulses et al., 2023), mainly conducted at the time-series DYFAMED (43.42 ºN, 7.87 ºE; Marty, 2002) and BOUSSOLE sites (43.37° N, 7.90° E; Antoine et al., 2006, 2008a, 2008b). These investigations have shown the seasonal cycle of the surface CO_2 is primarily governed by thermal fluctuations and the behaviour of the area as a relatively weak sink for atmospheric CO_2 on an annual scale. Long-term changes estimated by Merlivat et al., (2018) reported the increase in the surface CO_2 fugacity ($fCO_{2,sw}$) and pH of ~40 µatm and ~0.04 units, respectively, since the 90s decade. The interannual trends given for $fCO_{2,sw}$ (2.3 ± 0.23 µatm yr^{-1}; Merlivat et al., 2018) and pH (0.002-0.003 units yr^{-1}; Yao et al., 2016) were in agreement with those encountered in the Northeast Atlantic at the ESTOC site (2.1 ± 0.1 µatm yr^{-1} and 0.002 ± 0.0001 units yr^{-1}, respectively; González-Dávila and Santana-Casiano, 2023). Long-term variations in MCS within the northwestern Mediterranean occur at rates exceeding those anticipated from chemical equilibrium with atmospheric CO_2, which has been attributed to the intense deep-convection processes in this area (Copin-Montégut, 1993; D'Ortenzio et al., 2008; Cossarini et al., 2021) and the substantial input of anthropogenic carbon from the North Atlantic (Merlivat et al., 2018; Palmiéri et al., 2015; Schneider et al., 2010; Ulses et al., 2023). Based on a high-resolution regional model, Palmiéri et al., (2015) estimated that ~25% of the anthropogenic carbon storage in the Mediterranean Sea comes from the Atlantic. The water exchange processes in the Strait of Gibraltar become the western boundary of the Mediterranean Sea in a crucial region for MCS variability which significantly modulates the basin-wide anthropogenic carbon inventory and ocean acidification trends in the Mediterranean basin and could affect significantly the general circulation and the composition of seawaters in the North Atlantic. Additionally, this region is subject to variability related with (1) the intense deep-water convection in the adjacent Northwestern area of the Mediterranean Sea and (2) the unique circulation patterns shaped to the irregular coastlines and islands, which forms quasi-permanent eddies and other (sub)mesoscale features (Alberola et al., 1995; Bosse et al., 2021; 2016; Bourg and Molcard, 2021).

This research focus on the surface spatio-temporal variations of the MCS and air-sea CO_2 fluxes in the western boundary of the Mediterranean Sea. High-resolution and reliable data were obtained through autonomous underway monitoring of the surface ocean from February 2019 to February 2024 by a Volunteer Observing Ship (VOS). This systematic strategy represents a powerful tool to analyse the distribution and changes of physical and MCS properties in highly variable areas as coastal transitional zones where the availability of data has been historically scarce. The cruise track (Figure 1) followed the south and east geographically rugged coastline of the Iberian Peninsula and allowed the characterization of the Alboran Sea (~2-5.1ºW) separately from the eastern coastal and shelf area between Cape of Gata (Almería) and Barcelona (~36.5-41.3ºN). The changes observed in the MCS on a seasonal and interannual timescales (even considering the limitations of 5 years of data), the mechanism controlling their variations and the changes in the air-sea CO_2 exchange have been attended in this study.

2. Material and methods

2.1. Study area

The Western boundary of the Mediterranean Sea encompasses the Alboran Sea, land-loaded by the southern Iberian Peninsula coast and northern African coast, and the coastal transitional area along the eastern Iberian margin (Figure 1a). The classical surface circulation pattern in the Alboran Sea (e. g. Bormans and Garrett, 1989; Peliz et al., 2013; Sánchez-Garrido et al., 2013, 2022; Speich, 1996; Whitehead and Miller, 1979), with the Atlantic water jet (AJ) following wavelike path of the quasi-permanent Western Anticyclonic Gyre (WAG) and the Eastern Anticyclonic Gyre (EAG) and constituting the Modified Atlantic Water (MAW; Lopez-García et al., 1994; Viúdez et al., 1998), drive west-to-east variations in physical and biogeochemical terms. The intensity and direction of the AJ, depending primarily on sea level pressure and local wind fluctuations, variate on different timescales and govern the circulation patterns in the Alboran Sea influencing the biogeochemistry (Sánchez-Garrido and Nadal, 2022; Solé et al., 2016). On a seasonal scale, the AJ oscillate between two main circulation modes (García-Lafuente et al., 2002; Macías et al., 2008, 2016; Vargas-Yáez et al., 2002), detectable by reanalysis data-based SST signals (Figure 1b): a high-intense AJ flowing north-eastward during spring/summer and a lower-intense AJ flowing with more south-eastwardly direction during autumn/winter. The stronger AJ during the warm months feed the classical two-gyres configuration in the Alboran Sea, while the weak AJ only allows the existence of the WAG (Renault et al., 2012). The AJ forms a filament flowing from the Iberian coastal upwelling in the northwestern Alboran Sea and surrounding the eastern edge of the WAG, which is most frequently presented during summer (Gómez-jakobsen et al., 2019; Millot, 1999). The westernmost part of the Alboran Sea is affected by the shallow position of the Atlantic-Meridional Interface layer (AMI; Bray et al., 1995; Lacombe and Richez, 1982), which promotes the injection of deep-water into the surface (Echevarría et al., 2002; Gómez-jakobsen et al., 2019; Minas et al., 1991).

The eastern Iberian margin is influenced by the path of the Northern Current transporting Mediterranean Water (MW; Pinot et al., 1995), which is originated around the Gulf of

Lion where the forcing of the northeasterly winds is frequently strong and flows southward along the eastern coastline of the Iberian Peninsula (Conan and Millot, 1995; Millot, 1999; Sammari et al., 1995). The seasonality of the Northern Current (Millot, 1999) infers meridional variations in the thermal signals between cold and warm months (Figure 1b). The enhanced wind-forcing during winter intensify the Northern Current, which fit to the Iberian continental slope and recirculate offshore at Cape of Nao (Millot, 1999), while a low-intense branch progress southward Cape of Nao and reach the eastern Alboran Sea. During summer, the weakening in the wind-forcing forms a surface thermal front in the axis of the Pyrenees, which was detectable in the reanalysis-based SST map (Figure 1b). This front changes the path of the Northern Current further away from the Iberian coast (Lopez-García et al., 1994), which allow the MAW to reach its northern most spreading. The interaction of the Northern Current with the variety of mesoscale features (mainly meanders and eddies) and the variations in stratification within the annual cycle introduced spatio-temporal differences in the biogeochemical properties (Bosse et al., 2021; Millot, 1999). Additionally, although terrestrial and riverine inputs have a less pronounced impact on biogeochemistry compared to the eastern Mediterranean basin (Cossarini et al., 2015), they can act as a source of local variability. The most significant in this area is the Ebro river runoff, which peaks in March-May due to the combined action of precipitation during winter and snowmelt in the upper river basins during spring (Zambrano-Bigiarini et al., 2010). It feed the coastal area around the Ebro Delta with fresh and cool waters (see in minimum SST compared to adjacent waters in February; Figure 1b).

2.2. Data collection

A high spatio-temporal resolution dataset spanning 5 years was constructed based on weekly physico-chemical observations of the surface western boundary of the Mediterranean Sea between February 2019 and February 2024. Data was automatically collected by the Volunteer Observing Ship (VOS) MV JONA SOPHIE (IMO: 9144718, called RENATE P before November 2021), a container ship managed in Spain by Nisa Maritima which links the Canary Islands with Barcelona. This VOS line was designed and is maintained by the QUIMA research group at the IOCAG-ULPGC, and operates within the framework of the Integrated Carbon Observation System (ICOS; https://www.icos-cp.eu/; last assess: 15 May 2025) as a Ship-of-Oportunity (SOOP) Ocean Station (Station ID: ES-SOOP-CanOA) since 2021 (upgraded to an ICOS Class 1

Ocean Station in May, 2024). Therefore, the measurement equipment and underway data collection techniques verify the ICOS high-quality requirements and methodological recommendations.

The ES-SOOP-CanOA station allows the monitoring of a coastal transitional zone transect across the western Mediterranean Sea (Figure 1), together with a northeast Atlantic subtropical area (Curbelo-Hernández et al., 2021a) and the Strait of Gibraltar (Curbelo-Hernández et al., 2021b). In the Alboran Sea, the vessel advanced eastward and longitudinally crossed the WAG through its northern part and followed the northern path of the EAG. The irregular southeast and east coastline of the Iberian Peninsula caused local differences in the oceanographic features and variances in the distance-to-land of the vessel track.

The system operates fully unattended in underway mode, with biweekly (time required to complete a round trip) routine maintenance at the port of Las Palmas de Gran Canaria (28.13 ºN, 15.42 ºW). Data is automatically transferred to a server when the vessel docks at each of the port along the usual route (Las Palmas de Gran Canaria, Santa Cruz de Tenerife, Arrecife, Sagunto and Barcelona). A total of 92 routes were completed in the Mediterranean Sea (Figure 1).

2.3. Monitoring routines

The autonomous underway monitoring of CO_2 in surface ocean (water intake placed at 5 m depth) and low atmosphere (air intake placed at 8 m above sea level) and the data collection routines followed the recommendations described by Pierrot et al., (2009) to ensure comparable and high-quality datasets. An automated underway CO_2 molar fraction (xCO_2, ppm) measurement system, developed by Craig Nail and commercialized by General Oceanics™, was installed inside the engine room of the vessel and described by Curbelo et al. (2021a, 2021b).

The xCO_2 measurement system combines an air and seawater equilibrator, placed inside the wet box, with a non-dispersive infrared analyser for gas detection, placed inside the dry box. The analyser used for xCO_2 detection was built by LICOR® (initially LI-6262 model and after October 2019, LI-7000 model). The nominal accuracy of the LICOR infrared gas analyser given by the manufacturer is 1% for CO_2 concentrations within the range of 0 to 3000 ppm. The system performs in-loop, at 3-minute intervals, five measurements of atmospheric xCO_2 ($xCO_{2,atm}$) and eighty measurements of surface seawater xCO_2 ($xCO_{2,sw}$). The $xCO_{2,atm}$ data was consistent with daily $xCO_{2,atm}$ records from the Izaña Atmospheric Research Center (IZO site located in Tenerife, Canary Islands, Spain; 28.3090ºN, 16.499ºW, placed at 2372.9 m above sea level; https://gml.noaa.gov/dv/site/site.php?code=IZO, last access: 14 May 2025), which is operated by the Spanish Meteorological Agency (AEMET) and forms part of several major international atmospheric monitoring networks (Figure Sup1). Daily $xCO_{2,atm}$ data from IZO are available through the National Ocean and Atmospheric Administration (NOAA) Global Monitoring Laboratory (GML) dataset (https://gml.noaa.gov/data/dataset.php?item=izo-co2-flask; last access: 14 May 2025). During 2019-2024, $xCO_{2,atm}$ measurements from ES-SOOP-CanOA station were, on average, 1.14 ppm higher than those recorded at IZO (Figure Sup1), which may be attributed to the fact that air sampling at IZO is conducted at approximately 2400 meters above sea level, in a remote location far from major urban or industrial areas and above the atmospheric inversion layer, which shields the station from surface-level pollution. In contrast, the ES-SOOP-CanOA measurements are conducted in the lower atmosphere, near the sea surface and closer to greenhouse gas emission sources (particularly when the vessel operates near the coast in the Mediterranean basin).

The LICOR® analyser is automatically calibrated on departure and arrival at each port and periodically every three hours using four standard gases. Additionally, the system is zeroed and spanned (with standard gases 1 and 4, respectively) every twelve hours to properly interpolate the standard values and correct for instrument drift. The four standard gases, with an accuracy of ±0.02 ppm, were provided by the NOAA and traceable to the World Meteorological Organization (WMO). They were in the order of 0 ppm, 250 ppm, 400 ppm and 550 ppm until January 2021, when the gas bottles for standard 2 to 4 were changed for a new set with concentrations in the order of 300 ppm, 500 ppm and 800 ppm provided by the ICOS central analytical laboratories.

The sea surface temperature (SST, in ºC) was monitored by using a SBE38 thermometer placed at the primary seawater intake in the engine room, with a reported instrumental error of ±0.01ºC. The high sensitivity of xCO_2 to temperature fluctuations required the monitoring of temperature at different locations across the system. A SBE45 thermosalinograph and a Hart Scientific HT1523 Handheld Thermometer, with reported instrumental errors of ±0.01ºC, were used to monitor the seawater temperature at the entrance of the wet box and inside the equilibrator, respectively. The measured SST was analysed in conjunction with SST reanalysis monthly data (0.042º x 0.042º; with dates spanning 24 years within 01/01/2000 and 01/03/2024) from the Med MFC physical multiyear product (Escudier et al., 2020; 2021; Nigam et al., 2021), available at Copernicus Marine Data Store (https://data.marine.copernicus.eu/products; last access: 15 May 2025). The SST reanalysis data was interpolated to the coordinates of the ES-SOOP-CanOA data to perform direct comparison in their dynamics.

The Sea Surface Salinity (SSS) was measured by the SBE45 thermosalinograph, whose instrumental error fall in the order of ±0.005. Lastly, pressure is measured within ±0.0002 atm at the deck box transducer close to the air intake (used as atmospheric pressure), in the wet box inside the equilibrator at the time of equilibration and in the dry box to be used by the LICOR analyser to correct the analog signal for any pressure effects.

Discrete surface seawater samples were manually collected with in situ records of SST and SSS during three round trips in February 2020, March 2021 and October 2023 (a total of 102 were collected in the Mediterranean Sea). The discrete sampling was performed along the vessel track from the seawater supply line every 1-2 hours in borosilicate glass bottles, overfilled and preserved with 100 µl of saturated $HgCl_2$. Samples were kept in dark and analysed just after arriving at port, in a period less than 2 weeks, for total alkalinity (A_T, µmol kg^{-1}).

The underway observational dataset exhibits a gap of a year between September 2021 and 2022 due to the temporary cessation of the measurement system for vessel maintenance in dry dock. During this period, the measurement system was sent for calibration and maintenance to General Oceanics enterprise, Miami, USA. There are also several gaps of less than a month related with different technical issues with the measurement equipment, which were addressed during the routine maintenance visits to the vessel (i. e. problems with the pump and seawater intake, with the LICOR analyser, depletion of gas bottles supplies, electrical issues in the engine room). Certain technical issues encountered during 2020 were delayed in being resolved due to the constraints imposed by COVID-19.

2.4. Calculation procedures

2.4.1. CO_2 system variables

The present investigation followed the data collection methodology, quality control and calculation procedures as published in the updated version of the DOE method manual for ocean CO_2 analysis (Dickson et al., 2007). The correction of the measured xCO_2 and calculation of the fugacity of CO_2 (fCO_2) in surface seawater ($fCO_{2,sw}$) and atmosphere ($fCO_{2,atm}$) followed the procedure described by Pierrot et al. (2009). This procedure avoids significant uncertainties in the determination of fCO_2 arising from differences in pressure and temperature conditions between sampling (atmospheric pressure and SST) and equilibration (pressure and seawater temperature inside the equilibrator once equilibration is reached). By calibrating the instrument with standard gases ranging from 0 to 800 ppm (which encompasses the measurement range of 300 to 600 ppm) and actively minimizing temperature and pressure drift through continuous monitoring (see Section 2.3 for standard gas, temperature, and pressure accuracies), the system achieved the target accuracy of ±0.2 µatm for $fCO_{2,atm}$ and ±2 µatm for $fCO_{2,sw}$ (Pierrot et al. 2009). The full set of standard gases was linearly interpolated to the time of observations to generate the calibration curve used for xCO_2 correction before calculating fCO_2.

The raw output data was initially filtered removing data affected by the automatic sampler such as samples measured at low water rates (< 2.0 L min^{-1}) and/or samples in which the difference in temperature between the seawater intake and the equilibrator was higher than 1.5ºC. The outliers, assumed as elements more than three local standard deviations from the local mean over a window length of fifty elements, were also removed from the dataset. The xCO_2 measured values in low atmosphere after each calibration were averaged and interpolated at the times of each xCO_2 observation in seawater by applying a piecewise polynomial-based smoothing spline.

The discrete seawater samples were analysed for A_T by using a VINDTA 3C and following the procedure detailed by Mintrop et al., (2000). The VINDTA 3C was calibrated through the titration of Certified Reference Material (CRMs; provided by A. Dickson at Scripps Institution of Oceanography), giving values with an accuracy of ±1.5 µmol kg^{-1}. A new approach to reconstruct A_T using salinity-based empirical relationship was built specifically for the monitored transect. The A_T-SSS linear relationship obtained from 46 discrete samples (Eq. 1) is statistically significant at the 99% level of confidence (p-value < 0.01) and present a high degree of correlation (r^2= 0.99) and a RMSE of ±5.6 µmol kg^{-1}. The propagated uncertainty in A_T estimates, considering the errors in A_T

determination and SSS measurements (Section 2.3) and the linear model uncertainty, was approximately ±5.7 µmol kg^{-1}. This error in A_T estimation falls within the accepted uncertainty range of ±10 µmol kg^{-1} for A_T when used as an input variable alongside $fCO_{2,sw}$ (when its uncertainty is up to ±2 µatm) for the calculation of other MCS variables aligning with the criteria for the "weather goal" level of measurement quality (Steinhoff and Skjelvan, 2020).

This linear relationship aligns with those proposed in various zones of the Mediterranean Sea (Schneider et al., 2007, Copin-Montégut and Bégovic, 2002, Jiang et al., 2014, Cossarini et al., 2015). Although the reconstruction of A_T from its linear relationship with SSS does not account for biological processes that cannot be traced with salinity (Wolf-Gladrow et al., 2007), nor the input of dissolved carbonate minerals and bicarbonate-carbonate species from river runoff, sediments, and water mixing, it has been widely used and provides a useful general approximation in regions with stable conditions and less influenced by these processes. Considering that the influence of biological cycles on A_T is reduced along the western boundary of the Mediterranean Sea due to the influx of cooler and nutrient-rich Atlantic waters, and that terrestrial and riverine contributions have minimal influence on A_T distribution compared to marginal and coastal areas in the Eastern Mediterranean Basin (Cossarini et al. 2015), the A_T was calculated at the times of the observations (Curbelo-Hernández et al., 2021a; 2021b; 2023) using Eq. 1. This new A_T-SSS relationship can be used to calculate the A_T content in surface seawaters subject to low influence of non-salinity factors in the western Mediterranean Sea, with salinities ranging between 36 and 38.5.

$$A_T = 100.5\ (\pm 2.9)\ SSS - 1271(\pm 108) \tag{1}$$

The pH and C_T were calculated at the times of the underway observations by using the CO_{2SYS} programme developed by Lewis and Wallace, (1998) and run with the MATLAB software (van Heuven et al., 2011; Orr et al., 2018; Sharp et al., 2023). The $fCO_{2,sw}$ and A_T were used as input CO_2 system variables. The set of constant used for computations includes the carbonic acid dissociation constants of Lueker et al., (2000), the HSO_4 dissociation constant of Dickson, (1990), the HF dissociation constant of Perez and Fraga, (1987) and the value of $[B]_T$ determined by Lee et al., (2010). The effect of temperature on pH was removed by computation at a constant temperature of 19ºC, which is the mean temperature within the observational period (referred as pH_{19}). Further data adjustments and statistical procedures are detailed in Appendix A.

2.4.2. Thermal and non-thermal $fCO_{2,sw}$

The relative influence of the thermal and non-thermal processes on the variation of $fCO_{2,sw}$ has been addressed. The non-thermal processes mainly include the biological and carbonate pumps, circulation patterns and air-sea gas exchange (De Carlo et al., 2013). The collectively known methodology presented by Takahashi et al., (2002) with the experimentally-determined temperature effects on pCO_2 for isochemical seawater of 0.0423 $°C^{-1}$ (Takahashi et al., 1993) was used. This procedure has been previously applied to ES-SOOP-CanOA data and detailed by Curbelo-Hernández et al., (2021a; 2021b). An alternative procedure recently introduced by Fassbender et al., (2022) and detailed by Rodgers et al., (2023), modified from the Takahashi et al., (2002, 1993) framework, was also applied in this investigation. This updated method addresses the slightly variations in the thermal sensitivity of $fCO_{2,sw}$ due to background chemistry (Wanninkhof et al., 1999, 2022), which introduces slightly difference between the observed seasonal cycle of $fCO_{2,sw}$ and the calculated through the sum of its thermal and non-thermal components. The Takahashi et al. (2002) and Fassbender et al. (2022) procedures are referred hereinafter as T'02 and F'22, respectively.

The new approach in F'22 for the thermal component of $fCO_{2,sw}$ ($fCO_{2,\ T\ FASS}$) was computed from the annual means (denoted with the subscripts AM) of SSS, A_T and C_T at in situ temperature (Eq. 2) by using the CO_{2SYS} programme (Lewis and Wallace, 1998) for MATLAB (van Heuven et al., 2011; Orr et al., 2018; Sharp et al., 2023). Then, the thermal-driven change in $fCO_{2,sw}$ ($fCO_{2,\ T\ anom}$) can be calculated as the difference between the thermal component of $fCO_{2,sw}$ ($fCO_{2,\ T\ FASS}$) and the annual mean of $fCO_{2,sw}$ (Eq. 3).

$$fCO_{2,\ T\ FASS} = CO_{2,SYS}(C_{T,AM},\ A_{T,AM},\ SSS_{AM}, SST) \quad (2)$$

$$fCO_{2,\ T\ anom} = fCO_{2,\ T\ FASS} - fCO_{2,AM} \quad (3)$$

The new approach in F'22 for the non-thermal component ($fCO_{2,\ NT\ FASS}$) is given by the difference between the $fCO_{2,sw}$ at the times of observations and the $fCO_{2,\ T\ anom}$ (Eq. 4).

The difference among $fCO_{2,\ NT\ FASS}$ and the annual mean of $fCO_{2,sw}$ provides the change in $fCO_{2,sw}$ explained by non-thermal processes ($fCO_{2,\ NT\ anom}$) (Eq. 5).

$$fCO_{2,\ NT\ FASS} = fCO_{2,sw} - fCO_{2,\ T\ anom} \tag{4}$$

$$fCO_{2,\ NT\ anom} = fCO_{2,\ NT\ FASS} - fCO_{2,\ AM} \tag{5}$$

Considering the seasonal amplitudes of $fCO_{2,T}$ and $fCO_{2,NT}$ ($dfCO_{2,T}$ and $dfCO_{2,NT}$), the relative importance of thermal and non-thermal processes was expressed by the T/B ratio ($dfCO_{2,T}/dfCO_{2,NT}$), with values greater than 1 indicating that the temperature effect govern the $fCO_{2,sw}$ variations.

2.4.3. Factors controlling the seasonal amplitude of $fCO_{2,sw}$

The changes in the surface $fCO_{2,sw}$ result from the combined variation in the physical and biochemical seawater properties. The seasonal variability of the surface $fCO_{2,sw}$ was addressed by attending the partial contribution of SST, SSS, C_T and A_T (e. g. Takahashi et al., 2014). The influence of each driver was quantified by assuming linearity and employing a first-order Taylor-series deconvolution (Sarmiento and Gruber, 2006) given in Eq. 6 and previously used for pCO_2 (Doney et al., 2009; Lovenduski et al., 2007; Takahashi et al., 1993; Turi et al., 2014) and pH (Fröb et al., 2019; García-Ibáñez et al., 2016; Pérez et al., 2021; Takahashi et al., 1993; Curbelo-Hernández et al., 2024).

The seasonal changes of each driver (SST, SSS, C_T and A_T) in Eq. 7 $\left(\frac{dX}{dt}\right)$ were assumed as their difference between the times of the year in which $fCO_{2,sw}$ was at its minimum and maximum (seasonal amplitudes) per months elapsed. Seasonal amplitudes were calculated between monthly means (based on observations and computed data) for February and September (where minimum and maximum $fCO_{2,sw}$ were observed). An error propagation based on standard deviations for February and September was performed to calculate the error of the seasonal change.

Due to the high relevance of the evaporation/precipitation processes in the Mediterranean Sea and in order to avoid the influence of freshwater fluxes, the most recent equation (Eq. 7) given by Pérez et al., (2021) with salinity-normalized C_T and A_T (NC_T and NA_T) was used. The normalization was performed to a constant salinity (SSS_0) of 37.4 ($NX_T = SSS_0 * X_T / SSS$), which is the average SSS for the entire monitored area.

$$\frac{dfCO_2}{dt} = \frac{\partial fCO_2}{\partial SST}\frac{dSST}{dt} + \frac{\partial fCO_2}{\partial SSS}\frac{dSSS}{dt} + \frac{\partial fCO_2}{\partial C_T}\frac{dC_T}{dt} + \frac{\partial fCO_2}{\partial A_T}\frac{dA_T}{dt} \tag{6}$$

$$\frac{dfCO_2}{dt} = \frac{\partial fCO_2}{\partial SST}\frac{dSST}{dt} + \left(\frac{\partial fCO_2}{\partial SSS} + \frac{NC_T}{SSS_0}\frac{\partial fCO_2}{\partial C_T} + \frac{NA_T}{SSS_0}\frac{\partial fCO_2}{\partial A_T}\right)\frac{dSSS}{dt} + \frac{SSS}{SSS_0}\frac{\partial fCO_2}{\partial C_T}\frac{dNC_T}{dt} + \frac{SSS}{SSS_0}\frac{\partial fCO_2}{\partial A_T}\frac{dNA_T}{dt} \tag{7}$$

It is important to remark that the changes in NA_T and NC_T are linked with biogeochemical processes which have different influences: the processes involved in the organic carbon pump contribute to strongly change the NC_T weakly affecting the NA_T, while those involved in the carbonate pump affect the NA_T twice as much as NC_T. The positive values of $\frac{dfCO_2}{dt}$ and $\frac{\partial fCO_2}{\partial X}\frac{dX}{dt}$ indicate an increase in $fCO_{2,sw}$ from February to September, while negative values the opposite.

2.4.4. Air-sea CO_2 fluxes

The air-sea CO_2 fluxes (FCO_2) were determined using the bulk formula (Broecker and Peng, 1983) in Eq. 8:

$$FCO_2 = 0.24\, K_0\, K_{660}\, \Delta fCO_2 \tag{8}$$

where K_0 is the solubility of CO_2 in seawater, K_{660} is the gas transfer velocity and ΔfCO_2 represents the difference between $fCO_{2,sw}$ and $fCO_{2,atm}$. A conversion factor of 0.24 was used to express FCO_2 values in units of mmol m^{-2} d^{-1}. K_0 was calculated by using the equation and coefficients given by Weiss, (1974) and measured SST and SSS which fall within the valid application limits. Considering the fitting error from the original parameterization of K_0 ($\pm 1\times 10^{-4}$ mol L^{-1} atm^{-1}; Weiss, 1974) and the instrumental errors of SST and SSS measurements (section 2.3), the uncertainty associated with the solubility estimation had a negligible impact on the calculation of FCO_2. K_{660} was calculated through its quadratic dependency with wind speed (Eq. 9) using the parametrization given by Wanninkhof (2014):

$$K_{660} = 0.251 \cdot \mathrm{w}^2 \cdot \left(\frac{\mathrm{Sc}}{660}\right)^{-0.5} \tag{9}$$

where w is the wind speed and Sc is Schmidt number (cinematic viscosity of seawater, divided by the gas diffusion coefficient). ERA5 hourly wind speed reanalysis data at 10 m above the sea level and with a spatial resolution of 0.25º x 0.25º (Hersbach et al., 2023) were used to calculate K_{660}. The ERA5 reanalysis for the global climate and weather is available at Copernicus Climate Data Store (https://cds.climate.copernicus.eu/; last access: 15 May 2025). The uncertainty in K_{660} reported by Wanninkhof (2014) when using wind speeds ranging between 3 and 15 m s^{-1} is ±20%. The error in the determination of $fCO_{2,sw}$ and $fCO_{2,atm}$ (Section 2.4.1) propagates into the calculation of ΔfCO_2 and constitutes an additional source of uncertainty. The statistical procedure used to quantify the uncertainty in the FCO_2 arising from the uncertainty in ΔfCO_2 is described in Appendix B. The mean absolute error in FCO_2 due to the propagated uncertainty of ΔfCO_2 (±2.01 µatm) was ±0.14 mmol m^{-2} d^{-1}, which in relative term is ±0.05%. Negative FCO_2 values indicate that the ocean acts as an atmospheric CO_2 sink, while the positive ones indicate that it behaves as a source.

3. Results

A total amount of 157,984 data for surface ocean xCO_2 were collected during the study period (34,015 data during 2019, 28,590 data during 2020, 33,288 data during 2021, 19,102 data during 2022, 39,738 data during 2023 and 3,251 data during January and February 2024). This amount exceeds the total number of data points available in the historical record for the Western Mediterranean (34.8-43.1ºN, 5.5ºW-4.7ºE) since 1999 (146,094 data) available in SOCAT v2024 (Bakker et al., 2016, 2024). The total number of data points in this region included in the SOCAT v2024 database since 2019 is 44,520.

Due to differences in the spatial distribution of observations, two subregions (referred to as sections) were identified along the vessel track (Figure 1): the longitudinally distributed southern section (hereinafter S section), accomplishing the Alboran Sea (~2-5.1ºW), and the latitudinally distributed east section (hereinafter E section), following the eastern coastline of the Iberian Peninsula (~36.5-41.3ºN). The spatiotemporal distribution of $fCO_{2,sw}$ and the total number of data points available in each dataset for sections S and E is shown in Figure Sup2. In the S section, $fCO_{2,sw}$ values from ES-SOOP-CanOA station are consistent with those in SOCAT v2024, although the limited number of cruises covering this section in SOCAT v2024 difficult a direct comparison and prevent robust characterization of spatial and seasonal variability patterns. In the E section, some differences between the two datasets are observed (i. e. during spring–summer 2021, $fCO_{2,sw}$ was higher in SOCAT v2024 than in the ES-SOOP-CanOA dataset). These differences are mainly explained by the distinct sampling trajectories in SOCAT v2024, with some routes extending further eastward, including coastal areas around the Balearic Islands.

The spatial distribution of the average values allowed to identify heterogeneity in the annual cycle of each variable along both sections (Figure 2 and Sup3). The standard deviation of the spatially-averaged variables is presented in Table Sup2. A strong west-to-east increasing gradient in SST was observed in summer through the S section (~5.5ºC) which lead an increment in $fCO_{2,sw}$ of ~57.5 µatm and a depletion in pH of ~0.040 units eastward across the Alboran Sea. Despite the approximately constant SST through the S section during the rest of the year (less than 1.5ºC of difference between the western and easternmost parts), an eastward decrease in $fCO_{2,sw}$ of less than 18 µatm accompanied by an increase in pH of less than 0.030 units was observed between October and March.

The latitudinal gradient of SST through the E section was weaker throughout the year, keeping spatially stables the $fCO_{2,sw}$ and pH. The maximum change in SST occurs during winter, in which a northward decrease of less than 2ºC explained minimum seasonal average temperatures and $fCO_{2,sw}$ through the cruise track (14-15 ºC and 350-360 µatm, respectively). It contrasts with the maximum average temperatures and $fCO_{2,sw}$ encountered during summer (25.0-26.5 ºC and 450-470 µatm, respectively). These results reported that the maximum amplitude of the seasonal cycle of SST, $fCO_{2,sw}$ and pH occurs along the eastern coastline of the Iberian Peninsula and specially over the continental shelf between Valencia and Barcelona (northernmost part of E section), while the minimum seasonal amplitude occurs near the Strait of Gibraltar (westernmost part of the S section).

The spatial variation in C_T were significant throughout the year along both sections (Figure 2). The C_T increases eastward in the order of 20-45 µmol kg^{-1} along the S section throughout the year. This increment accelerated along the E section from Cape of Gata to Cape of Nao and become approximately stable from Cape of Nao to Barcelona port. The spatial distribution of C_T was highly influenced by the progressively salinification observed along the S section. The SSS increased during the entire annual cycle from 36.3-36.5 around the eastern part of the Strait of Gibraltar to 37.7-38.1 around Cape of Nao

(Figure Sup3). Removing the effect of salinity, the NC_T (Figure Sup3) presents a weaker spatial variation through the vessel track mainly lead by biological and mixing processes.

The surface physico-chemical properties show heterogeneities during some seasons of the year among several key locations along the sections (Figure 2 and Sup3). The heterogeneities in the temporal evolution of the SST, SSS and CO_2 system variables was assessed by the strategic selection of 5 stations along the S section (stations S1-S5) and 6 stations along the E section (stations E1-E6), geographically depicted in Figure 1. The S1 (4.95 ± 0.05 ºW) occupied the easternmost part of the Strait of Gibraltar, the S2-S4 (4.35 ± 0.05 ºW, 3.85 ± 0.05 ºW and 2.95 ± 0.05ºW) were placed in the central Alboran Sea and the S5 (2.45 ± 0.05 ºW) located south of Cape of Gata. The stations along the E section include E1 (37.1 ± 0.2 ºN) in the Gulf of Mazarron, E2 (37.6 ± 0.2 ºN) to the east of Cape of Palos, E3 (38.2 ± 0.2 ºN) in the Gulf of Alicante, E4 (38.7 ± 0.2 ºN) to the east of Cape of Nao, E5 (39.3 ± 0.2 ºN) in the Gulf of Valencia over the continental slope, and E6 (40.2 ± 0.2 ºN) near the Ebro estuary over the continental shelf.

The temporal variations of each variable at S1-S5 and E1-E6 are depicted in Figure 3, 4, Sup4, Sup5 and Sup6. The seasonal amplitudes and interannual trends are summarized in Table 1. The seasonal amplitude of SST (minimum values in February-March around 14-17 ºC and maximum values in August-September around 20-26ºC) increased eastward through the S section although the local decrease at S2 (Figure 3 and Sup4, Table 1). The seasonal changes were larger through the E section (~14 to ~28ºC) and show weaker spatial variations (Figure 4 and Sup5, Table 1). The SSS (Figure Sup6), do not exhibit a seasonal cycle well-correlated to the harmonic function in Eq. A.1 ($r^2 < 0.5$; Table Sup2). The lower and more spatially stable SSS values were observed along the S section during the entire period (around 36.0-37.5), while increase with latitude through the E section (around 36.7-38.1).

The seasonal amplitude of $fCO_{2,sw}$ (from ~340 to ~460 µatm in the S section and from ~340 to ~470 µatm in the E section) and pH (from ~8.00 to ~8.12 units in the S section and from ~8.00 to ~7.98 to ~8.13 units in the E section) was strongly linked with those of SST. It exhibits a west-to-east increment through the S section with the exception at S2 (Figure 3 and Sup4, Table 1) and remained approximately constant through the E section (Figure 4 and Sup5, Table 1). These spatial heterogeneities in the seasonal cycles were found to be leaded by the different rise in SST during late summer along each section as minimal spatial differences were observed during the rest of the year.

The C_T (Figure Sup6) seasonally decreased from January-February to September-October (from ~2180 to ~2085 µmol kg^{-1} in the S section and from ~2260 to ~2105 µmol kg^{-1} in the E section) in phase with the enhancement biological production. The seasonal amplitude of C_T increased eastward through the S section and northward through the E section, following the salinification gradient (Figure Sup6, Table 1). Once removed the effect of salinity, the seasonal cycle of NC_T shows minimal differences in the S section between the western and the easternmost part, while in the E section the NC_T and its seasonal amplitude increased northward (Figure Sup6, Table 1). The enhanced adjustment (correlation) of NC_T with Eq. A.1 ($0.47<r^2<0.61$ at S section and $0.70<r^2<0.88$ at E section) compared to C_T ($0.28<r^2<0.56$ at S section and $0.45<r^2<0.73$ at E section) emphasizes the relevance of the processes variating salinity. The lower correlations encountered through the S section shows the higher impact of eventual processes (i. e. changes in the evaporation/precipitation, river runoff, mesoscale features) locally modifying the surface carbon system in this area and introducing spatial heterogeneities in their seasonal cycles.

4. Discussion

4.1. Spatial characterization of the CO_2 system and its seasonality

4.1.1. The Alboran Sea

The seasonal variability of the AJ (García-Lafuente et al., 2002; Macías et al., 2008, 2016; Vargas-Yáez et al., 2002) modified the SST signature in the S section, thus influencing $fCO_{2,sw}$ and pH. The maximum intensity of the AJ during summer (Peliz et al., 2013; Renault et al., 2012) caused a more intense warming and salinification of MAW while advancing into the Mediterranean Sea and mixing with the fraction of MW which surround the Cape of Gata and recirculate westward (Millot, 1999; Sánchez-Garrido et al., 2013). It explained the eastward increase in $fCO_{2,sw}$ and decrease in pH at this time of the year (Figure 2; Section 3.1).

The relatively low SST and $fCO_{2,sw}$ around S1 (20.68 ± 2.20 ºC and 401.68 ± 27.13 µatm) and S3 (21.15 ± 2.11 ºC and 407.30 ± 26.20 µatm) were mainly due to the highest intensity of the wind-induced upwelling along the northern coast of the western Alboran

Sea during the warm season. It cooled the surface and enhanced the biological drawdown (e. g. Bolado-Penagos et al., 2020; Folkard et al., 1997; Gómez-Jakobsen et al., 2019; Peliz et al., 2009; Richez and Kergomard, 1990; Stanichny et al., 2005), while favouring the formation of the cold and nutrient-rich filament separating the WAG and EAG (Gómez-Jakobsen et al., 2019; Millot, 1999). Differences in the influence and strength of this filament may contributed to the observed heterogeneities in SST, $fCO_{2,sw}$, and pH at S1 during the warm seasons (Figure 3), which in turn account for reducing the model fitting performance. Additionally, the shallowest position of the AMI during late-winter (De La Paz et al., 2009; Echevarría et al., 2002; Gómez-Jakobsen et al., 2019; Minas et al., 1991) feed the surface with CO_2-rich waters coming from deeper areas in the Mediterranean Sea (De La Paz et al., 2009; Echevarría et al., 2002; Gómez-Jakobsen et al., 2019; Minas et al., 1991), elevating $fCO_{2,sw}$ around S1. The increase in C_T and NC_T during summer around S3 (Figure 2 and Sup3), which contributed to reduce their seasonal amplitudes in this area (Figure Sup6, Table 1), suggests that the upwelled waters transported by the filament at this time of the year were not enough remineralized to compensate the SST-driven decrease in $fCO_{2,sw}$. In consequence, the western and eastern edges of the WAG presented the shortest seasonal amplitudes along the S section for SST, $fCO_{2,sw}$ and pH (Figure 3; Table 1).

Conversely, the increase in SST and $fCO_{2,sw}$ during summer around S2 (22.63 ± 2.05 ºC and 429.98 ± 24.86 µatm), S4 (23.89 ± 2.03 ºC and 438.25 ± 25.22 µatm) and S5 (24.05 ± 1.61 ºC and 441.67 ± 16.22 µatm) contributed to extend their seasonal amplitudes in these zones (Figure 2 and 3; Table 1). It suggest that, during the warm season, the increase in $fCO_{2,sw}$ leaded by the surface warming near the core of the gyres was not compensated by the biological drawdown occurring at this time of the years (which caused a weak decrement in C_T and NC_T at S2; Figure 2 and Sup3).

4.1.2. The Eastern Iberian margin

The eastern coastal transitional area of the Iberian Peninsula was subject to variability related with changes in the intensity, morphology and path of the Northern Current (Figure 1b). The SST decreased in the northernmost part of the E section from Sagunto to Barcelona throughout the year (north of S5; Figure 2). The cooling of this area intensified during the cold season due to the mixing of warm waters in the wind-shielded area North of Cape of Nao with cool and salty MW transported by the Northern Current.

However, it weakened during the warm season due to the northward spreading of MAW favoured by the formation of the thermal front in the axis of the Pyrenees, changing the path of the Northern Current (López-García et al., 1994). In the southernmost part of the section, the enhanced northward spreading of MAW and less wind stress during summer drives the warming observed from Cape of Gata (at S5) to Cape of Nao (at E4), while a low intense branch of the Northern Current transporting MW and progressing southward Cape of Nao weakly cool the area during winter (López-García et al., 1994; López-Jurado et al., 1995).

The local decrease in SST and $fCO_{2,sw}$ observed during the warm seasons at E4 traced the offshore recirculation of the Northern Current at Cape of Nao (Millot, 1999) and separating the E section within its northern and southernmost areas. This division was also evidenced based on the C_T and NC_T signatures (Figure 2 and Sup6): the northernmost part of the section receives remineralized MW transported by the Northern Current which elevates C_T and NC_T, while the southernmost part was supplied with recent MAW with relatively low C_T and NC_T. Additionally, Ulses et al. (2023) recently suggested that the convective area in the Gulf of Lion behaves as a source of natural and anthropogenic carbon to the intermediate waters of the western Mediterranean, which can enter the surface through vertical mixing and account for the observed high amount of C_T and NC_T.

Although the spatial heterogeneities and the northward cooling during the cold season (Figure 1) increasing seasonal changes in SST, the seasonal amplitudes of $fCO_{2,sw}$ keep approximately constant within E1-E6 (Figure 3 and Sup5; Table 1). The location of station E5, away from the influence of the Northern Current during the warm months, explained its locally lower seasonal amplitudes compared to adjacent waters in the northernmost part of E section. Nevertheless, these heterogeneities were minimal and do not caused differences in the seasonal amplitude of pH (Table 1).

In the case of C_T and NC_T (Figure Sup6, Table 1), the enhancement in the mixing of MAW with MW during winter increased northward the seasonality from E1 to E4. In the northernmost part, the seasonal variations in C_T and NC_T become shorter due to their increment during the cold season. It was caused by the combined action of the enhanced arrival of remineralized MW at this time of the year and the mesoscale structures locally favouring injections of CO_2-rich deeper waters into the surface (Bosse et al., 2021; Millot, 1999). The Ebro River runoff peaking among late-winter and spring (Zambrano-Bigiarini et al., 2010) can also behaves as a source of variability around E5-E6.

4.2. Warming and interannual trends of MCS variables

The monitoring of the surface Western Mediterranean Basin allowed the identification of interannual trends for physical and MCS properties (Table 1 and 2). The SST increased at a rate of 0.38 ± 0.05 ºC yr^{-1} in the S section and 0.30 ± 0.04 ºC yr^{-1} in the E section. The rate of increase in SST locally intensified at S2 (0.50 ± 0.09 ºC yr^{-1}) may be due to the transport and accumulation of surface waters toward the core of the WAG. Its variability, migration and progressively collapse can also account for the rapid warming of the area (Sánchez-Garrido et al., 2013; Viúdez et al., 1998; Vélez-Belchí et al., 2005).

The SST trends based on ES-SOOP-CanOA data were of the same order of magnitude as those derived from reanalysis data for the period 2019–2024, but were one order of magnitude higher than the reanalysis-based trends for 2000–2019, indicating a reinforcement of sea surface warming by approximately 80–90% (Table 1). The ES-SOOP-CanOA data-based interannual SST trends were found to be reinforced during summer by 55.2% in the S section and by 32.4% in the E section compared to winter. The Northern Current cooling the northernmost part of the E section accounted to decelerate the warming in comparison to the S section. The ES-SOOP-CanOA data-based trends reported a cumulative increase in SST from 2019 to 2024 of 1.91 ± 0.26 ºC in the Alboran Sea (S section) and 1.52 ± 0.22 ºC along the eastern Iberian margin (E section). These cumulative increments were 48.3% and 34.94% respectively higher than those estimated for the global surface ocean from 1850-1900 to 2001-2020 (0.99 ± 0.12 ºC; IPCC, 2023). It aligns with projections from climate models for both terrestrial and marine environments in the mid latitudes, particularly within the Mediterranean region, in consequence of human-induced global warming, which was detailed by Hoegh-Guldberg et al., (2018) in the AR6 Synthesis Report (IPCC, 2023).

The warming contributes to modify the MCS dynamics, mainly accelerating the increase in $fCO_{2,sw}$ and acidification. The interannual trends of $fCO_{2,sw}$ and pH (Table 1) were more than twice (except for trends at S1) than those reported for the Northwestern Mediterranean at the DYFAMED site based on the difference between average observation-based data for the periods 1995-1997 and 2013-2015 (2.30 ± 0.23 µatm yr^{-1}

and -0.0022 ± 0.0002 units yr^{-1}; Merlivat et al., 2018) and for the Northeast Atlantic at the ESTOC site based on in situ measurements since 1995 (2.1 ± 0.1 µatm yr^{-1} and 0.002 ± 0.0001 units yr^{-1}, respectively; González-Dávila and Santana-Casiano, 2023). The interannual rates accelerated eastward along the S section and northward along the E section (Table 1). The stronger trends at S3 compared to adjacent waters (S2 and S4) may be due to the transport of CO_2-rich waters from the southern Iberian coast through the filament. The trends in the S section were conducted by the larger rates of change encountered during the warm season compared to the cold season. The opposite occurred in the E section, where an intense increase in $fCO_{2,sw}$ accompanied by a drawdown in pH occurred during winter and trends were reversed during summer (Table 1).

These spatial differences among the cold and warm seasons were mainly linked with variations in the biological production/remineralization and mixing and were independent of the surface ocean warming. Hence, they were required to be assessed together with the NC_T trends for a better understanding. The NC_T interannually decreases throughout the region (Table 2). The rapid depletion in the S section during winter in comparison to summer could be due to, first, an interannual weakening in remineralization processes and/or inputs of CO_2-rich water to the area during the cold months, and second, an interannual strengthened in the biological uptake during the warm months. However, these variations resulted insufficient to compensate the increase in $fCO_{2,sw}$ and subsequent fall down in pH induced by warming during the cold and even more during the warm months. Conversely, in the E section, the variations in lateral/vertical advection, primary driven variations in the (sub)mesoscale structures (Alberola et al., 1995; Bosse et al., 2021; 2016; Bourg and Molcard, 2021), were of high-relevance and introduced differences in the annual cycle of NC_T. The interannual variations during winter were minimal (Table 1, Figure Sup6), likely due to not significant changes in remineralization and in the dissolved CO_2 concentration of waters transported into the area. The decrease in NC_T intensified during summer (Table 1, Figure Sup6) likely caused by the enhancement in biological production together with the dismissing lateral advection (this may be related with a reinforcement in the front formed in the axis of the Pyrenees due to the increasingly higher SST of the MAW).

Once removed the effects of temperature, the interannual pH_{19} trends overturned to negligible and were not statistically significant in the S section (<-0.001 units yr^{-1}; p-values > 0.1). It suggests that warming is directly driving the acidification (and indirectly by rising $fCO_{2,sw}$) while the progressively enhancing in biological productivity partially compensates for the expected fall down in pH. In the E section, pH_{19} were reduced by 63% (-0.002 ± 0.001 units yr^{-1}; p-values < 0.01) in comparison to the pH trends, which explains that the increase in SST is contributing more than half on the acidification due to only the atmospheric fCO_2 increase. The negative pH_{19} trends reinforced in the E section by 47% during the cold season due to the enhancement in remineralization. The pH_{19} trends reversed to positive during the warm season due to the important role of biological production actively reducing $fCO_{2,sw}$ and rising pH at this time of the year.

However, despite the high statistical confidence in the trends and the consistency found with reanalysis products, the acceleration in surface warming and consequent changes in $fCO_{2,sw}$ and pH observed may be linked to isolated extreme events such as marine heat waves and are not necessarily indicative of prolonged behaviours over time. The globally increased frequency and magnitude in marine heat waves in phase with warming (Oliver et al., 2018; Hoegh-Guldberg et al., 2018; Frölicher et al., 2018; Smale et al., 2019) could feedback and hence continue expediting the surface ocean warming. The influence of these extreme events is especially relevant in semi-enclosed seas as the Mediterranean, recognized as one of the most affected marine areas in the yearly Copernicus Ocean State Reports (OSR; EU Copernicus Marine Service; https://marine.copernicus.eu/access-data/ocean-state-report; last access: 15 May 2025) since 2016 (OSR1-OSR7).

4.3. The relative contribution of thermal and non-thermal processes on the surface $fCO_{2,sw}$

The temporal evolution of $fCO_{2,sw}$ due to thermal and non-thermal effect ($fCO_{2,T}$ and $fCO_{2,NT}$, respectively) showed a high degree of agreement between the T'02 and F'22 methodologies (Figures 3 and 4). The average $fCO_{2,T}$ and $fCO_{2,NT}$ values differed by less than 5 µatm between the two methodologies. The consistency with the widely employed T'02 engenders confidence in the validity and reliability of the most updated F'22 method.

The seasonal variations in $fCO_{2,sw}$ were close to twice in the E section compared to the S section (Table 1). The thermal-driven seasonal changes ($dfCO_{2,T}$) were found to approximately double those independent of temperature ($dfCO_{2,NT}$) throughout the region

(Table 2). The T/B ratios demonstrated the control of thermal processes over the seasonality of $fCO_{2,sw}$ throughout the region (Table 2). The T/B ratios in the westernmost part of the S section (ranged between 1 and 2) were consistent with previous studies in the Strait of Gibraltar (Curbelo-Hernández et al., 2021b; De La Paz et al., 2009). The T/B ratios increased eastward as the AJ advanced in the Alboran Sea and caused by the intense increase in $dfCO_{2,T}$ compared to $dfCO_{2,NT}$. They exceeded 2 in S4-S5 and E1-E6, which demonstrated the larger control of SST over $fCO_{2,sw}$ in areas less influenced by the input of surface Atlantic water.

The interannual trends show the control of thermal processes over the increase in $fCO_{2,sw}$ during 2019-2024 (Figure 3 and 4; Table 2). The strong and statistically significant interannual $fCO_{2,T}$ trends show the important role of warming in elevating $fCO_{2,sw}$. The weak and non-significant $fCO_{2,NT}$ trends suggest that spatio-temporal variations in the biological processes, circulations patterns and air-sea gas exchange introduced local differences in the distribution of $fCO_{2,sw}$. It difficult to assess the impact of the non-thermal processes on an interannual scale at each of the stations. The interannual trends of $fCO_{2,T}$ and $fCO_{2,NT}$ for the entire S and E sections (Table 2) were statistically significant at more than the 95% level of confidence and its coupling described, with less than 0.3 $\mu atm\ yr^{-1}$ of difference (<1%), the interannual rates of $fCO_{2,sw}$ during 2019-2024 (Table 1; section 4.2).

The thermal processes govern the changes in $fCO_{2,sw}$ on an interannual scale with a contribution ranged between ~76-92% in the S section and ~73-83% in the E section. The contributions for $fCO_{2,NT}$ were between ~8-25% and ~17-27%, respectively. The decrease in $fCO_{2,NT}$ compensated by ~6-30% the increase in $fCO_{2,sw}$ at S1-S5 and E1-E2, while its increase contributed by ~24-53% to rise $fCO_{2,sw}$ at E3-E6. The negative $fCO_{2,NT}$ trends in the S section were related to progressive enhancement in the biological uptake (mainly during spring/summer) not compensated by remineralization and/or vertical/lateral advections of remineralized waters (mainly during autumn/winter) in areas influenced by recent MAW. Conversely, the interannual increase in $fCO_{2,NT}$ in the E section suggest that the supply of cool and remineralized MW along the path of the high-intense Northern Current surpasses the biological drawdown of surface CO_2 and is accounting to accelerate the increase in $fCO_{2,sw}$ on an interannual scale.

4.4.Mechanism controlling the seasonal cycle of $fCO_{2,sw}$

To infer the causes of variations in the seasonal cycle of $fCO_{2,sw}$ among the study period, the seasonal rates of change in $fCO_{2,sw}$ ($\frac{\mathrm{d}fCO_{2,sw}}{\mathrm{dt}}$, hereinafter d$fCO_2$) were decomposed into their individual components ($\frac{\partial fCO_{2,sw}}{\partial X}\frac{\partial X}{\mathrm{dt}}$, hereinafter d$fCO_2^X$) as described in section 2.4.3 (Eq. 6 and 7). The results of solved Eq. 7 for each year at S1-S5 and E1-E6 are depicted in Figure 5. The uncertainty associated with the difference between the monthly means for each term and year was obtained through error propagation considering their individual standard errors and presented in Table Sup 3. The dfCO_2 resulted from the cumulative sum of the individual terms in Eq. 7 (indicated with subscript "sum") matched the dfCO_2 directly calculated from observations between both seasons (indicated with the subscript "obs"), which renders confidence to the methodology (Figure 5).

The SST was identified as the main driver of dfCO_2, describing 45-78% and 55-83% of its changes in the S and E sections, respectively. In the S section (Figure 5a), dfCO_2^{SST} increased westward as MAW get warmed in the Alboran Sea, while the incursion of the filament locally cooled the surface and decreased dfCO_2^{SST} at S3. In the E section (Figure 5b), dfCO_2^{SST} increased northward and reach its maximum north of Cape of Nao (at E4-E6), particularly during 2021-2022 (32.0-32.5 µatm month^{-1}), due the higher influence of warmed MW.

The A_T has a low influence on increasing dfCO_2 in the entire region (<15%). As the $fCO_{2,sw}$ inversely changes with A_T, the weakly negative dfCO_2^{AT} found for some years along the S section show fluctuations in the periods of increment and decrement of A_T likely related with changes in the mixing processes. The A_T contribution becomes negligible at E6 (<1%) due to the minimal seasonal amplitude of A_T and NA_T (Figure Sup6). The approximately constant A_T and NA_T levels throughout the year may be due to the bicarbonate and carbonate content from the Ebro River runoff being neutralized by those in MW and MAW, which spread into the area during winter and summer, respectively. dfCO_2^{AT} tend to decrease since 2020-2021 in S1-S3, S5 and E1 due to the progressively weakening in the NA_T depletion from February to September. The opposite occurred north of Cape of Palos, where the seasonal cycle of NA_T reaches its maximum amplitude (20-27 µmol kg^{-1} at E3 and E4). The interannual dealkalinization in S and E sections (Table 1) behaves as a source of heterogeneities: the interannual negative NA_T trends during the cold months (p-values < 0.01) were stronger than during the warm months (p-values > 0.1) and consistent in both sections. The spatial differences in the summer trends (weaker in the S compared to E section) account for an enhanced reduction of the seasonal amplitude of NA_T in the S section.

The d$f$$CO_2^{SSS}$ were minimal in both the S and E sections (<0.7 and < 1.9 µatm month^{-1}, respectively) and show the weak impact of SSS over d$f$$CO_2$ (<3.5%). The entrance of MAW and its mixing with saltier MW in the Alboran Sea do not allow to identify a seasonal pattern in SSS (Figure Sup6), thus explained the negligible contribution of SSS in the S section (~2.3% at S1 which fall down to <1.0% at S2-S5). The larger seasonal amplitudes of SSS at E1-E5 (Figure Sup6) led a relatively major influence of SSS (~1.0-2.4% during most of the years). The low seasonal amplitude of SSS and A_T at E6, likely related with an approximately constant influence of the Northern Current at this location throughout the annual cycle, caused a minimal variation in d$f$$CO_2$ (<1%).

The depletion in C_T, mainly drove by the increased biological production from February to September, had a significant impact on d$f$$CO_2$ (25-38%). It compensates more than one third of the expected increase in d$f$$CO_2$ driven by SST and slightly prompt by A_T. In the S section (Figure 5a), the lower changes observed during the period of study in d$f$$CO_2^{CT}$ (4-6 µatm month^{-1}) compared to d$f$$CO_2^{SST}$ (6-9 µatm month^{-1}) demonstrated that fluctuations in C_T were increasingly insufficient to counterbalance the warming-driven increase in d$f$$CO_2$, even at S2-S4 where the biological production enhanced and hence the d$f$$CO_2^{CT}$ reinforced since 2020. In the westernmost part of the S section, the influence of C_T offsetting d$f$$CO_2$ was maximum during 2019-2020 at S1 (>84%), S2 (67.3%) and S3 (86.1%) and diminished toward 2023 (37.1%, 38.3% and 45.1%, respectively). In the easternmost part, this compensation was around 33-44% at S4-S5 throughout the period (as at S2 and S3 since 2020) except for 2023 at S5, in which d$f$$CO_2^{CT}$ weakened and offset only the 22.8%. In the E section (Figure 5b), the progressively strength in the processes depleting C_T throughout the period at E1-E4 and since 2020 at E5-E6 compensated by 33-46% the d$f$$CO_2^{SST}$, which changes inversely to d$f$$CO_2^{CT}$. The lowest compensation found in 2019 at E5 (28.8%) and E6 (18.4%) was likely related with eventual injections of remineralized waters along the Northern Current path, which offset the biological uptake of C_T and elevated the d$f$$CO_2^{CT}$.

4.5. Air-sea CO_2 exchange across the Western Boundary of the Mediterranean Sea

The continuous observation of MCS variables enabled the calculation of FCO_2 at an unprecedented high spatiotemporal resolution in the Western Mediterranean Sea. The FCO_2 was found to be governed by fluctuations in ΔfCO_2 (Figure 6), mainly controlled by the broader variability of $fCO_{2,sw}$ (325-500 µatm) compared to $fCO_{2,atm}$ (390-425 µatm). The SST fluctuations has a relevant role by primary controlling $fCO_{2,sw}$ (section 4.3) and modulating the solubility of CO_2 at the air-sea interface. The entire monitored area was undersaturated for CO_2 respect to the low atmosphere between late October and June (ΔfCO_2= -35.30 ± 8.97 µatm), acting as an atmospheric CO_2 sink (-2.56 ± 0.55 mmol m^{-2} d^{-1}) which peaks in winter (-4.53 ± 0.44 and -3.29 ± 0.31 mmol m^{-2} d^{-1} in S and E sections, respectively). During summer, the area was supersaturated for CO_2 (ΔfCO_2= 36.43 ± 0.35 µatm) and acted as a source, which was about three times more intense along the E section (1.70 ± 0.43 mmol m^{-2} d^{-1}) compared to the S section (0.57 ± 0.35 mmol m^{-2} d^{-1}).

The spatial differences in SST during warm months introduced heterogeneities in the seasonal outgassing among both sections: the higher SST during summer in the E section reduced the solubility and contributed to a higher increase in $fCO_{2,sw}$ respect to $fCO_{2,atm}$ (ΔfCO_2= 49.83 ± 0.32 µatm) compared to the cooler S sectiom (ΔfCO_2= 16.35 ± 0.14 µatm). The seasonality in the formation of the CO_2 sink and source in the Alboran Sea was consistent with previous studies in the Strait of Gibraltar (Curbelo-Hernández et al., 2021b; de la Paz et al., 2011, 2009) and Northwest African coastal transitional area in the Northeast Atlantic (Curbelo-Hernández et al., 2021a; Padin et al., 2010) and agreed with the seasonal pattern characteristic for tropical and subtropical regions (Bates et al., 2014; Takahashi et al., 2002). The warming during summer at S1 was insufficient to led supersaturated conditions (ΔfCO_2= -5.56 ± 0.26 µatm) and thus acted as a CO_2 sink throughout the year (-2.83 ± 1.77 mmol m^{-2} d^{-1} during cold months and -0.52 ± 0.02 mmol m^{-2} d^{-1} during the warm months), which coincided with the behaviour observed in the Strait of Gibraltar during 2019 (Curbelo-Hernández et al., 2021b). The sink and source status during cold and warm months encountered in the Eastern Iberian Margin agreed with FCO_2 evaluations based on observations in the Mediterranean basin through its northwestern (Wimart-Rousseau et al., 2023, 2021, 2020) and eastern parts (Sisma-Ventura et al., 2017), and confirms previous estimations based on satellite data and models (D'Ortenzio et al., 2008; Taillandier et al., 2012).

The variations in FCO_2 during the period of study were addressed by averaging the data across seasons and years at each of the selected stations (Figure 7). The same procedure was applied to ΔfCO_2 and wind speed (Figure Sup7 and Sup8). The evolution of the seasonal ingassing and outgassing was evaluated by computing interannual trends for average FCO_2 and ΔfCO_2 (Figure 7). The interannual FCO_2 trends evidenced the progressively strength of the summer source in the S section, which was accelerated at S2 in response to the enhanced warming around the WAG (detailed in section 4.2) and at S4-E1 due to their exposition to increasing wind forcing (Figure Sup7 and Sup8). It was caused by the increase in $fCO_{2,sw}$ during the warm months not offset by biological drawdown which elevated ΔfCO_2. In contrary, the localization of E2-E6 over the eastern Iberian continental shelf and slope allowed the relevant biological uptake at this time of the year to compensate for the influx of CO_2-rich water. It introduced heterogeneities in ΔfCO_2 between years which do not allow to identify statistically significant trends.

During spring and autumn, the increase in ΔfCO_2, mainly driven by warming, accompanied by the decreasing wind stress (Figure Sup7 and Sup8), led the positive interannual FCO_2 trends at S2-S5 and E1-E6 (Figure 7). They show the weakening in the ingassing during autumn and the achievement of a near-equilibrium state with the atmosphere during spring by the end of the study period. The FCO_2 reversed to weakly positive during spring 2023 in the E section, which prolonged the seasonal source period having a relevant impact on the net annual FCO_2. During winter, the increasing wind forcing compensated the reduction in the ingassing expected by the rise in ΔfCO_2 (Figure Sup7 and Sup8). However, the variability in the wind speed and other processes involved in the non-thermal change of $fCO_{2,sw}$ between years does not allowed the identification of statistically significant rates of change in the CO_2 sink status. Particularly, the relatively high wind speed during winter 2021 may have contributed to accelerated horizontal transports, increasing $fCO_{2,sw}$ and hence ΔfCO_2 (Figure Sup7 and Sup8).

The predominantly negative FCO_2 during most of the year led a net annual CO_2 sink behaviour. The positive FCO_2 trends during summer, spring and autumn have forced the annual average CO_2 invasion to decrease by 44-65% at S2-S5 (ranging from -0.66 ± 0.06 and -0.84 ± 0.04 mol m^{-2} during 2019 to -0.27 ± 0.09 and -0.47 ± 0.09 mol m^{-2} during 2023) and by 60-80% at E1-E6 (ranging from -0.32 ± 0.09 and -0.53 ± 0.09 mol m^{-2} during 2019 to -0.11 ± 0.10 and -0.13 ± 0.09 mol m^{-2} during 2023). The unique hydrodynamic of the Strait of Gibraltar strongly influenced the air-sea CO_2 exchange at S1: the ingassing during summer partially compensated for the reduction of the annual influx and resulted in a lower increase in FCO_2 (23%) from 2019 (-0.77 ± 0.02 mol m^{-2} yr^{-1}) to 2023 (-0.60 ± 0.06 mol m^{-2} yr^{-1}).

Considering the annual average FCO_2 for the S and E section, the net ingassing have decreased at a rate of 0.11 ± 0.02 mol m^{-2} yr^{-1} yr^{-1} (p-value<0.01) in the Alboran Sea and by 0.08 ± 0.02 mol m^{-2} yr^{-1} yr^{-1} (p-value<0.01) in the Eastern Iberian Margin. It contrast with the strength of the CO_2 sink across the western Mediterranean basin recently reported by Zarghamipour et al., (2024) for 1984-2019 based on a combination of observational data and model simulations (0.007 ± 0.001 mol m^{-2} yr^{-1} yr^{-1}). Additionally, Zarghamipour et al., (2024) noted the reduction of the annual net CO_2 source behaviour of the Central Mediterranean basin at an estimated rate of 0.003 ± 0.001 mol m^{-2} yr^{-1}. The findings suggest that the acceleration in the increase in $fCO_{2,sw}$ induced by the rapid warming, together with the progressive reduction in solubility, is reversing the interannual FCO_2 trends compared to previous decades, may be causing the study area to be resemble the Central and Eastern Mediterranean basin in terms of air-sea CO_2 exchange. The reduction of the net annual invasion was consistent with previous estimations in such coastal and shelf environments across the eastern tropical and subtropical South Atlantic during 2002-2018 (between 0.03 ± 0.01 and 0.09 ± 0.02 mol m^{-2} yr^{-1} yr^{-1}; Ford et al., 2022) and toward mid-latitudes over the Scotian Shelf (with average FCO_2 ranging from -1.7 mol m^{-2} yr^{-1} yr^{-1} in 2002 to -0.02 mol m^{-2} yr^{-1} yr^{-1} in 2006; Sisma-Ventura et al., 2017). The continuation of this decreasing rate for net annual ingassing would imply the reversion of the study area to a net annual CO_2 source behaviour before 2030.

The net CO_2 invasion was calculated by integrating the annual cycle of FCO_2 during 2019-2023. The net FCO_2 in the Alboran Sea was -1.57 ± 0.49 mol m^{-2} yr^{-1}, which represented a strength in the CO_2 sink in comparison with adjacent surface areas across the Strait of Gibraltar (between -0.82 and -1.01 mol m^{-2} yr^{-1} during 2019-2021; Curbelo-Hernández et al., 2021) and the Eastern Iberian Upwelling (-1.33 mol m^{-2} yr^{-1}; Chen et al., 2013). The net FCO_2 along the Eastern Iberian margin was -0.70 ± 0.54 mol m^{-2} yr^{-1}, which fall within the range of those modelled for the deep-convection area around the Bay of Marseille (Northwestern Mediterranean Basin) during 2012-2013 (-0.5 mol m^{-2} yr^{-1}; Ulses et al., 2023) and estimated based on observations during 2017-2018 (between

-0.26 and -0.81 mol m^{-2} yr^{-1}; Wimart-Rousseau et al., 2020). However, it was opposite to the net outgassing across the Easten Mediterranean basin (0.85 ± 0.27 mol m^{-2} yr^{-1} during 2009-2015; Sisma-Ventura et al., 2017). The net CO_2 sink for the monitored area across the Alboran Sea (14,000 Km^2) and eastern Iberian margin (40,000 Km^2) was -0.97 ± 0.30 Tg CO_2 yr^{-1} (-0.26 ± 0.08 Tg C yr^{-1}) and -1.22 ± 0.95 Tg CO_2 yr^{-1} (-0.33 ± 0.25 Tg C yr^{-1}). These findings powerfully contributed to the assessment of the air-sea CO_2 exchange in the Mediterranean basin and global coastal and shelf areas.

5. Conclusion

The five years of automatically underway observations at the ES-SOOP-CanOA Ocean Station provided a high spatio-temporal resolution dataset which includes the surface physical and MCS properties across the western margin of the Mediterranean Sea. It allowed the characterization, with an improved degree of certainty, of mechanisms involved in the MCS dynamics in the Alboran Sea and Eastern Iberian coastal transitional area on seasonal and interannual timescales.

The variations in $fCO_{2,sw}$ were found to be strongly controlled by temperature fluctuations. On a seasonal scale, the thermal-driven variations intensified as AJ advanced eastward in the Alboran Sea and MAW is formed, moved northward along the eastern Iberian margin and mixed with MW. In the Alboran Sea, the high intensity of the AJ during summer warms the surface layer toward the core of the WAG and EAG, driving larger seasonal changes in SST, $fCO_{2,sw}$ and pH which increased during the study period. The eastern Iberian margin was meridionally separated at Cape of Nao by the path of the Northern Current: the northernmost part, fed with cool, salty and remineralized MW during the cold season and influenced by the northward spreading of MAW during the warm season, show the largest seasonal amplitudes for SST, $fCO_{2,sw}$, and pH compared to the southernmost part, supplied with recent MAW during most of the year and by a weak and relatively warmed branch of the Northern Current during winter. The driver analysis has identified that 45-83% of the increase in $fCO_{2,sw}$ from February to September within the entire monitored area was explained by SST and <15% by AT and SSS, while the processes controlling C_T offsets 25-38% of this increment.

The changes in the seasonal cycles were driven, in first term, by the increasing contribution of temperature (due to the seasonal amplitude of SST is becoming larger) and, in second term, by the decreasing contribution of C_T (due to the dismissing remineralization/production ratio). On an interannual scale, the SST increased at rates ranging between 0.26 and 0.43 ºC yr^{-1} and drove a rapid increase in $fCO_{2,sw}$ within 4.18 and 5.53 µatm yr^{-1} and a decrease in pH within -0.0049 and -0.0065 units yr^{-1}. The ~76-92% of the interannual increase in $fCO_{2,sw}$ was described by warming. In the Alboran Sea and extending northward to Cape of Palos, non-thermal processes, primarily biological drawdown during spring blooms, compensated for up to one-third of the expected increase in $fCO_{2,sw}$ due to warming. The opposite occurred north of Cape of Palos, where non-thermal processes, mainly the inflow of CO_2-rich MW during the cold season, accounted for the increase in $fCO_{2,sw}$.

The assessment of the air-sea CO_2 exchange shows the Western boundary of the Mediterranean basin undersaturated and acting as a significant sink for atmospheric CO_2 during most of the year, while presented supersaturated conditions which led a CO_2 source status during the warm months. The entire monitored area acted as a net annual CO_2 sink, which is weakening at statistically significant rates ranging between 0.06 and 0.13 mol m^{-2} yr^{-1} yr^{-1} (40-80% since 2019). These trends would lead the area to shift towards becoming a net annual CO_2 source before 2030 if the current climate conditions persist. The weakening in the net annual CO_2 sink was driven by the ongoing strength of the summer outgassing (mainly in the Alboran Sea) and the weakening in the autumn and spring ingassing (throughout the region). Integrating the annual cycle of FCO_2 during the entire study period, the net CO_2 ingassing calculated for the Alboran Sea and Eastern Iberian Margin was -1.57 ± 0.49 and -0.70 ± 0.54 mol m^{-2} yr^{-1}.

This study highlights the need for systematic observation strategies to characterize the physico-chemical properties of seawater in the Mediterranean, an effort that has been required by the scientific community for the last decades. It demonstrates the effectiveness of SOOP/VOS for monitoring surface physical and biogeochemical variables, especially in highly variable and anthropogenically pressured areas such as coastal and semi-enclosed seas. The findings enhance our understanding of MSC dynamics in a key coastal transitional area of the Western Mediterranean, which is of high environmental and socio-economic importance and with implications for regional climate. Likewise, they contribute to a more accurate understanding of the role of coastal areas in the context of Global Change at both basin and global scales. Despite the relatively short study period, this research captured shifts likely driven by isolated events feedbacked by climate change, offering insights into future ocean conditions.

Appendix A: Data adjustments and statistical procedures

The temporal evolution of the physico-chemical data was analysed by weekly averaging (time required by the vessel to complete a trip) at different locations along the vessel track. The average values (y) were fitted to Eq. A.1 as a function of time (year fraction). This equation update the one used to study seasonal cycles by Curbelo-Hernández et al., (2021a; 2021b) through the addition of the $b\ (year - 2019)$ term, which provides the interannual rate of change of each seasonally-detrended variable between 2019 and 2024. The coefficients *a*-*f* and the standard errors of estimate given by Eq. A.1 for the variables considered are available in Table Sup1.

$$\mathrm{y} = \mathrm{a} + b\ (year - 2019) + \mathrm{c} \cdot \cos(2\pi\ \mathrm{year}) + \mathrm{d} \cdot \sin(2\pi\ \mathrm{year}) + \mathrm{e} \cdot \cos(4\pi\ \mathrm{year}) + \mathrm{f} \cdot \sin(4\pi\ \mathrm{year}) \tag{A.1}$$

The errors in the weekly averages were determined by dividing the Standard Deviation by the square root of the number of data points used to calculate the means ($Standard\ Deviation/\sqrt{n}$). The coefficient b in Eq. A.1 represented the interannual variation rates for each variable, which coincided with the slope derived from linear regressions of the detrended average values over time. The standard errors of these slopes were calculated by propagating the errors from the annual mean values.

The strength and direction of the linear regressions and the significance of the interannual trends was evaluated through the Pearson correlation test. This test yielded correlation coefficients (r^2) and corresponding p-values to determine statistical significance. Trends with p-values ≤ 0.01 were statistically significant at the 99% confidence level, those with p-values ≤ 0.05 were significant at the 95% confidence level, and trends with p-values ≤ 0.1 were significant at the 90% confidence level. Trends with p-values > 0.1 were not statistically significant but still provided an estimate of the temporal evolution of the variables within their respective layers.

Appendix B: Uncertainty in FCO_2 explained by the propagated error in ΔfCO_2

The uncertainty in $\Delta f CO_2$ was calculated by applying standard error propagation rules for the difference of two independent measurements with associated uncertainties (Eq. B.1):

$$\sigma_{\Delta f CO_2} = \sqrt{\sigma^2_{f CO_{2,sw}} + \sigma^2_{f CO_{2,atm}}} \qquad \text{B.1}$$

where $\sigma_{f CO_{2,sw}}$ and $\sigma_{f CO_{2,sw}}$ are the uncertainties for $fCO_{2,sw}$ and $fCO_{2,atm}$, respectively (see section 2.4.1). The absolute error in FCO_2 (σ_{FCO_2}; mmol m^{-2} d^{-1}) associated solely with uncertainty in $\Delta f CO_2$ was estimated for each data point using Eq. B.2:

$$\sigma_{FCO_2} = K_{660}\, K_0\, \sigma_{\Delta f CO_2} \qquad \text{B.2}$$

To represent the average magnitude of uncertainty in the estimated FCO_2 over the entire dataset (with *n* being the total number of data), the mean absolute FCO_2 error was calculated using Eq. B.3 and the mean relative FCO_2 was estimated with Eq. B.4:

$$\overline{\sigma_{FCO_2}} = \frac{1}{n}\sum_{i=1}^{n} \sigma_{FCO_{2},i} \qquad \text{B.3}$$

$$\frac{\overline{\sigma_{FCO_2}}}{FCO_2} = \frac{1}{n}\sum_{i=1}^{n} \left|\frac{\sigma_{FCO_{2},i}}{FCO_2}\right| * 100 \qquad \text{B.4}$$

Code Availability

The $CO_{2,SYS}$ programme for MATLAB is available at https://github.com/jonathansharp/CO2-System-Extd.

Data Availability Statement

The underway observations provided by the ES-SOOP-CanOA in the Western Mediterranean Sea (February 2019 – February 2024) used in this investigation are published in open-access at Zenodo (doi.org/10.5281/zenodo.13379011) and available since September 2023 at the ICOS Data Portal (https://www.icos-cp.eu/data-products/ocean-release). The SST reanalysis monthly data (0.042º x 0.042º) from the Med MFC physical multiyear product (Escudier et al., 2020; 2021; Nigam et al., 2021) are available at Copernicus Marine Data Store (https://data.marine.copernicus.eu/products). ERA5 hourly wind speed reanalysis data at 10 m above the sea level used to calculate air-sea CO_2 fluxes are available at Copernicus Climate Data Store (https://cds.climate.copernicus.eu/).

Author contribution

All the authors made significant contributions on this research. M. G.-D., J. M. S.-C. and A.G.G. installed and maintained the equipment in the VOS. D. C-H and D. G-S participated in routine maintenance and data acquisition. D. C.-H. developed the MATLAB® routines and conducted the data processing and analysis. All authors contributed to the writing of the manuscript and supported its submission.

Declaration Competing interest

The authors declare that the research was conducted in the absence of any commercial or financial relationships that could be construed as a potential conflict of interest.

Acknowledgement

This research was supported by the Canary Islands Government and the Loro Parque Foundation through the CanBIO project, CanOA subproject (2019–2024), and the CARBOCAN agreement (Consejería de Transición Ecológica y Energía, Gobierno de Canarias). We would like to thank the JONA SOPHIE ship owner, Reederei Stefan Patjens GmbH & Co. KG, the NISA-Marítima company and the captains and crew members for the support during this collaboration. Special thanks to the technician Adrian Castro-Álamo for biweekly equipment maintenance and discrete sampling of total alkalinity aboard the ship. We would like to thank the two anonymous reviewers for their constructive comments and suggestions, which have significantly improved the quality of this manuscript. The SOOP CanOA-VOS line is part of the Spanish contribution to the Integrated Carbon Observation System (ICOS-ERIC; https://www.icos-cp.eu/) since 2021 and has been recognized as an ICOS Class 1 Ocean Station. The participation of D. C-H was funded by the PhD grant PIFULPGC-2020-2 ARTHUM-2

Legend for Figures

Figure 1. (a) Map of the Western boundary of the Mediterranean Sea with the ES-SOOP-CanOA tracks between February 2019 and February 2024 (red) and the location of the stations of interest along the southern (S1-S5) and eastern (E1-E6) sections. The main Capes and Gulf along the geographically rugged Iberian coastline are shown. The schematic diagram summarized the classical circulation patterns: in the Alboran Sea (blue), the Atlantic Jet (AJ) surrounds the Western and Eastern Anticyclonic Gyres (WAG and EAG, respectively) and forms Modified Atlantic Water (MAW), while along the Eastern Iberian margin (purple), the Mediterranean Water (MW) is transported from the Northwestern Mediterranean basin along the path of the Northern Current. The northward spreading of MAW during summer and southward spreading MW during winter is depicted with dashed arrows. The thermal front formed in the axis of the Pyrenees during summer is depicted with a black dashed line. (b) SST maps built with reanalysis monthly data (0.042º x 0.042º) for February and September 2023 from the Med MFC physical multiyear product (Escudier et al., 2020; 2021; Nigam et al., 2021), available at Copernicus Marine Data Store (https://data.marine.copernicus.eu/products; last access: 15 May 2025).

Figure 2. Spatial distribution of the average SST, $f\text{CO}_{2,\text{sw}}$, pH, and C_T calculated on a seasonal and annual basis every 0.1º longitude along the S section (left panels) and every 0.25º latitude along the E section (right panels). The 3-months periods January-March, April-June, July-September and October-December were considered as winter, spring, summer and autumn, respectively. Note the different scales used for C_T due to significant variations between the S and E sections. Standard deviations are provided in Table Sup1 and indicate the range of variability among the study period.

Figure 3. Time-series of SST, $f\text{CO}_{2,\text{sw}}$ and pH at S1, S3 and S5 along the eastern Iberian margin within the five years of observations. The weekly average data was fitted to harmonic Eq. A.1. The thermal and non-thermal terms of the average $f\text{CO}_{2,\text{sw}}$ calculated by following the procedures of Takahashi et al., 2002 (T'02) and Fassbender et al., 2022 (F'22) and the pH_{19} are depicted. The coefficients *a-f*, standard errors of estimate and r^2 given by Eq. A.1 are presented in Table Sup1.

Figure 4. Time-series of SST, $f\text{CO}_{2,\text{sw}}$ and pH at E1, E4 and E5 in the Alboran Sea within the five years of observations. The weekly average data was fitted to harmonic Eq. A.1.

The thermal and non-thermal terms of the average $fCO_{2,sw}$ calculated by following the procedures of Takahashi et al., 2002 (T,02) and Fassbender et al., 2022 (F'22) and the pH_{19} are depicted. The coefficients *a-f*, standard errors of estimate and r^2 given by Eq. A.1 are presented in Table Sup1.

Figure 5. Temporal evolution of the seasonal rates of $fCO_{2,sw}$ explained by each of its drivers within the five years of observation. The differences between monthly average data for February and September (where minimum and maximum SST and $fCO_{2,sw}$ were encountered) was considered to compute the seasonal trends. The standard deviation of the monthly average data was considered in the calculation of the seasonal changes and infers errors in the computation of $fCO_{2,sw}$, which are summarized in Table Sup3. The cumulative $fCO_{2,sw}$ change ($\frac{\mathrm{d}fCO_{2,sw}}{\mathrm{dt}}$ (sum)) resulting from the distinct drivers were consistent with the observed seasonal $fCO_{2,sw}$ trends ($\frac{\mathrm{d}fCO_{2,sw}}{\mathrm{dt}}$ (obs)), thereby instilling confidence in the methodology.

Figure 6. Temporal variations of FCO_2 (blue; left axis), ΔfCO_2 (orange; right axis) and wind speed (gray; left axis) at (a) S1-S5 and (b) E1-E6. A piecewise polynomial-based smoothing spline was applied to the weekly average data (represented with dots). Gaps were covered by the harmonic fitting (Eq. A.1; dash line). The black lines represent the interannual increase in FCO_2. The seasonally-detrended interannual rates of change of FCO_2 and ΔfCO_2 are shown in each panel. *** denotes that the trends are statistically significant at the 99% level of confidence, ** at the 95% level of confidence and * at the 90% level of confidence. The wind speed does not show statistically significant interannual trends (p-values > 0.1).

Figure 7. Temporal evolution of average FCO_2 calculated on a seasonal and annual basis for each year (2019-2023) at S1-S5 and E1-E6. Same representation for ΔfCO_2 and wind speed is available in Figure Sup5 and Sup6. The 3-months periods January-March, April-June, July-September and October-December were considered as winter, spring, summer and autumn, respectively. The legend includes the interannual trends for FCO_2 (mol m^{-2} yr^{-1}) based on linear regression of the seasonal and annual means. *** denotes that the trends are statistically significant at the 99% level of confidence, ** at the 95% level of confidence and * at the 90% level of confidence. Standard deviations are presented in Table Sup4.

Legend for Tables

Table 1. Seasonal amplitudes and interannual trends of SST, SSS, $fCO_{2,sw}$, pH, pH_{19}, C_T and NC_T. The seasonal changes were calculated as the amplitude of Eq. A.1 fitted to the weekly average data at each station. The error of the seasonal amplitudes was assumed as the product of the standard error of estimate given by the harmonic function by 2. The interannual changes were based on linear regressions and given for each station and for the entire S and E sections (considering the total amount of average data at S1-S5 and E1-E6, respectively) during the cold and warm season. The interannual trends of SST during 2000-2019 (based on reanalysis monthly data from the Med MFC physical multiyear product [Escudier et al., 2020; 2021; Nigam et al., 2021]; detailed in section 4.2) was included for comparison. The trends were obtained by the linear regressions of the seasonally-detrended weekly average data and include their standard error of estimate. *** denotes that the trends are statistically significant at the 99% level of confidence, ** at the 95% level of confidence and * at the 90% level of confidence.

Table 2. Means, seasonal amplitudes and interannual rates of change of thermal and non-thermal components of $fCO_{2,sw}$ ($fCO_{2,T}$ and $fCO_{2,NT}$, respectively) calculated by following Takahashi et al., 2002 and Fassbender et al., 2022 (T'02 and F'22, respectively). The seasonal changes were calculated as the amplitude of Eq. A.1 fitted to the weekly average data at each station. The error of the seasonal amplitudes was assumed as twice the standard error of estimate given by the harmonic function. The trends were obtained by the linear regressions of the seasonally-detrended weekly average data and include their standard error of estimate. *** denotes that the trends are statistically significant at the 99% level of confidence, ** at the 95% level of confidence and * at the 90% level of confidence.

1107 Fig. 1

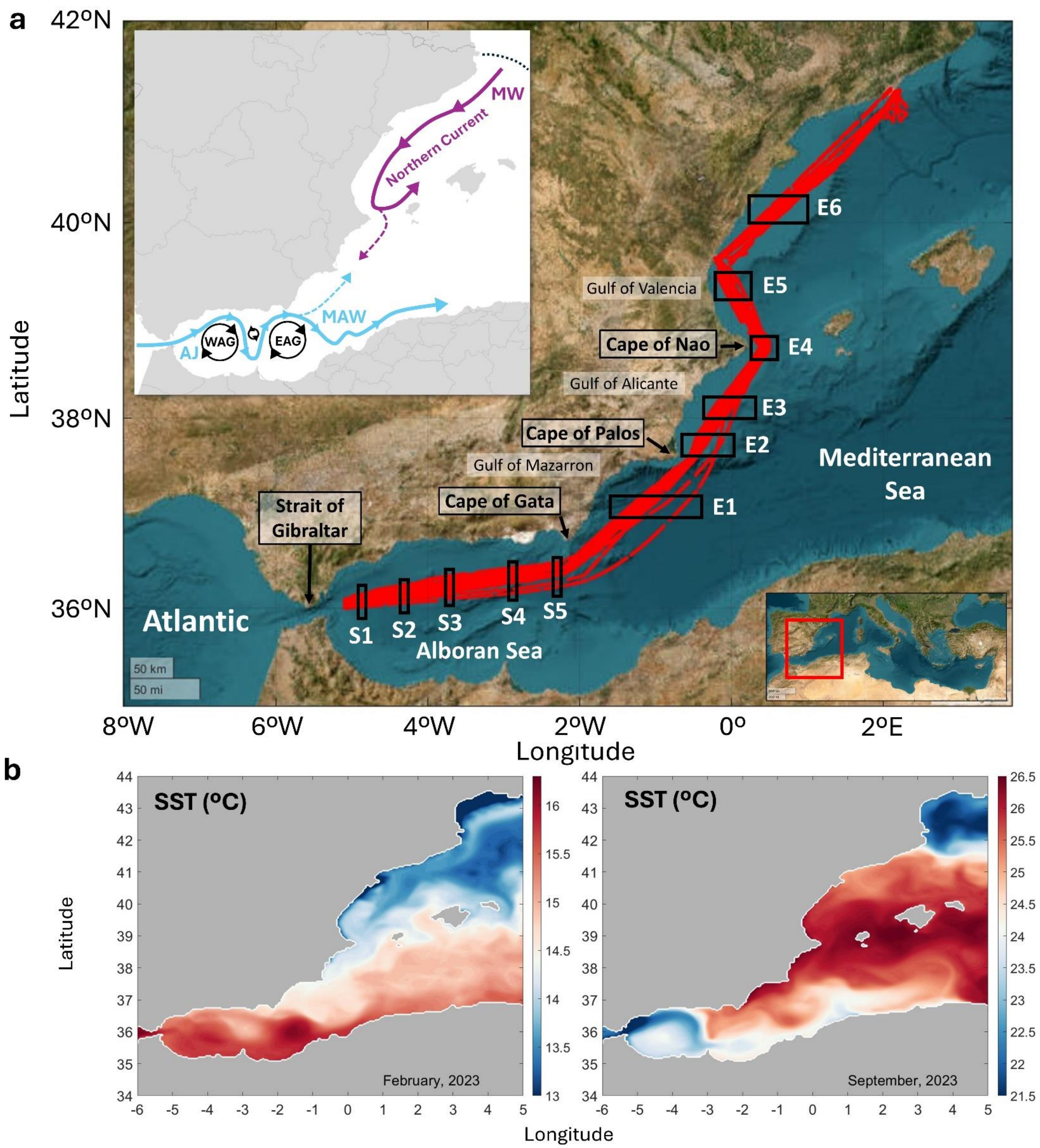
a
42ºN
40ºN
38ºN
36ºN
Latitude
8ºW
6ºW
4ºW
2ºW
0º
2ºE
Longitude
MW
Northern Current
MAW
AJ
WAG
EAG
E6
E5
E4
E3
E2
E1
Gulf of Valencia
Cape of Nao
Gulf of Alicante
Cape of Palos
Gulf of Mazarron
Cape of Gata
Strait of Gibraltar
Mediterranean Sea
Atlantic
S1
S2
S3
S4
S5
Alboran Sea
50 km
50 mi
b
SST (ºC)
February, 2023
SST (ºC)
September, 2023
Latitude
Longitude

1108 Fig. 2

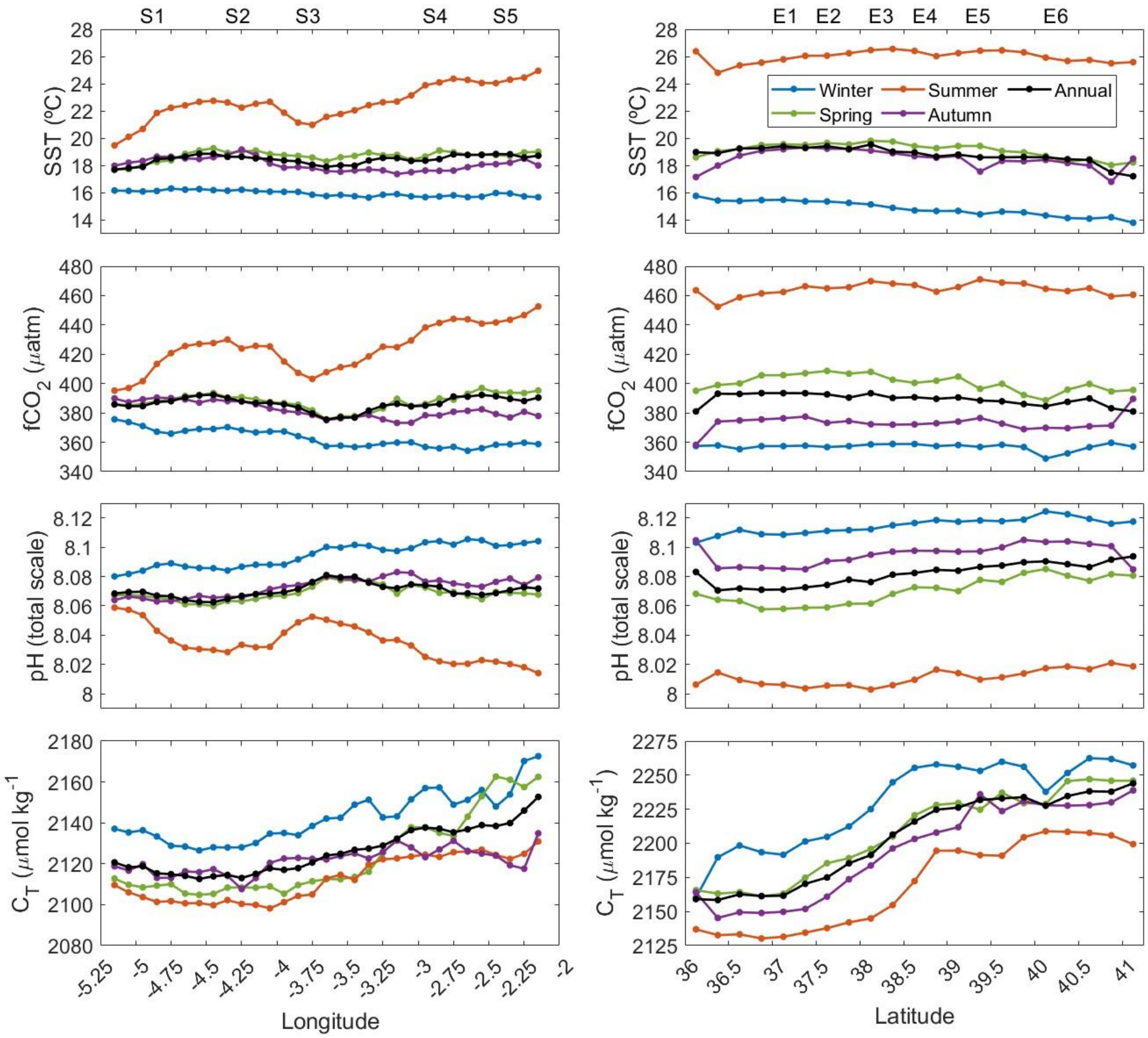

S1
S2
S3
S4
S5
E1
E2
E3
E4
E5
E6
Winter
Summer
Annual
Spring
Autumn
SST (ºC)
fCO2 (μatm)
pH (total scale)
CT (μmol kg-1)
Longitude
Latitude

1109 Fig. 3

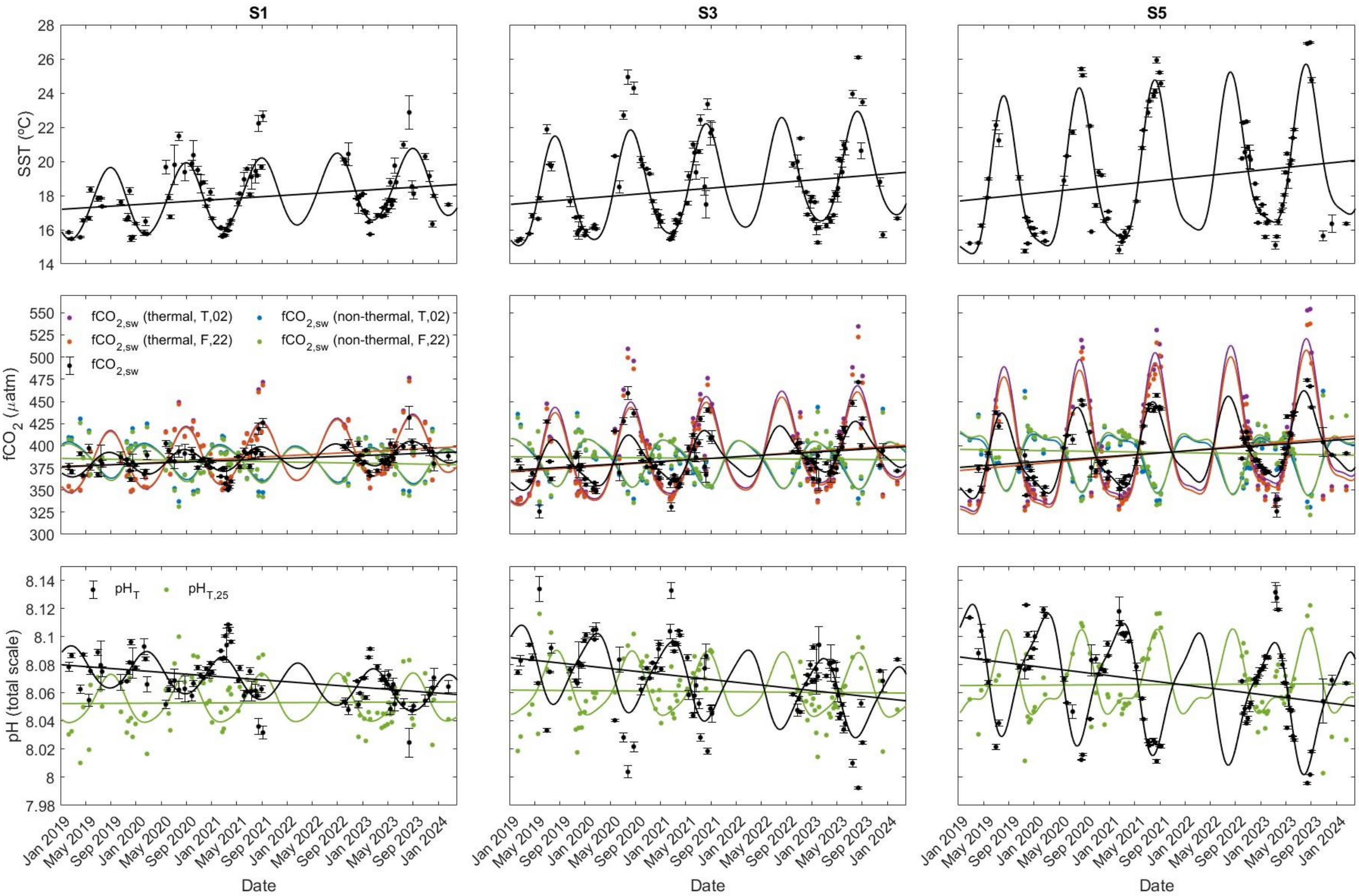

S1
S3
S5
SST (ºC)
fCO2,sw (thermal, T,02)
fCO2,sw (thermal, F,22)
fCO2,sw
fCO2,sw (non-thermal, T,02)
fCO2,sw (non-thermal, F,22)
fCO2 (µatm)
pHT
pHT,25
pH (total scale)
Date

Fig. 4

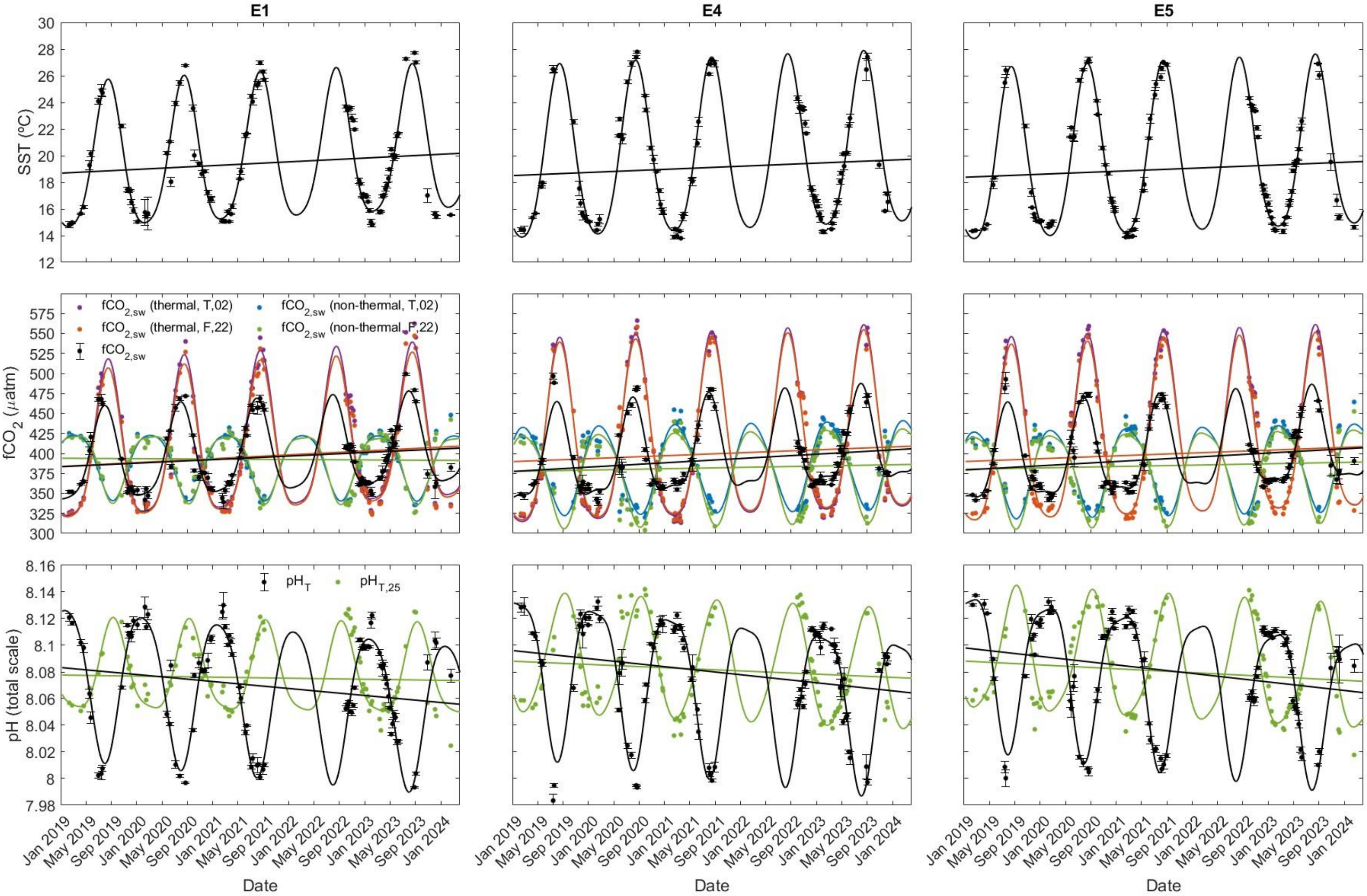

E1
E4
E5
SST (°C)
fCO2 (μatm)
fCO2,sw (thermal, T,02)
fCO2,sw (thermal, F,22)
fCO2,sw
fCO2,sw (non-thermal, T,02)
fCO2,sw (non-thermal, F,22)
pH (total scale)
pHT
pHT,25
Date

1111 Fig. 5

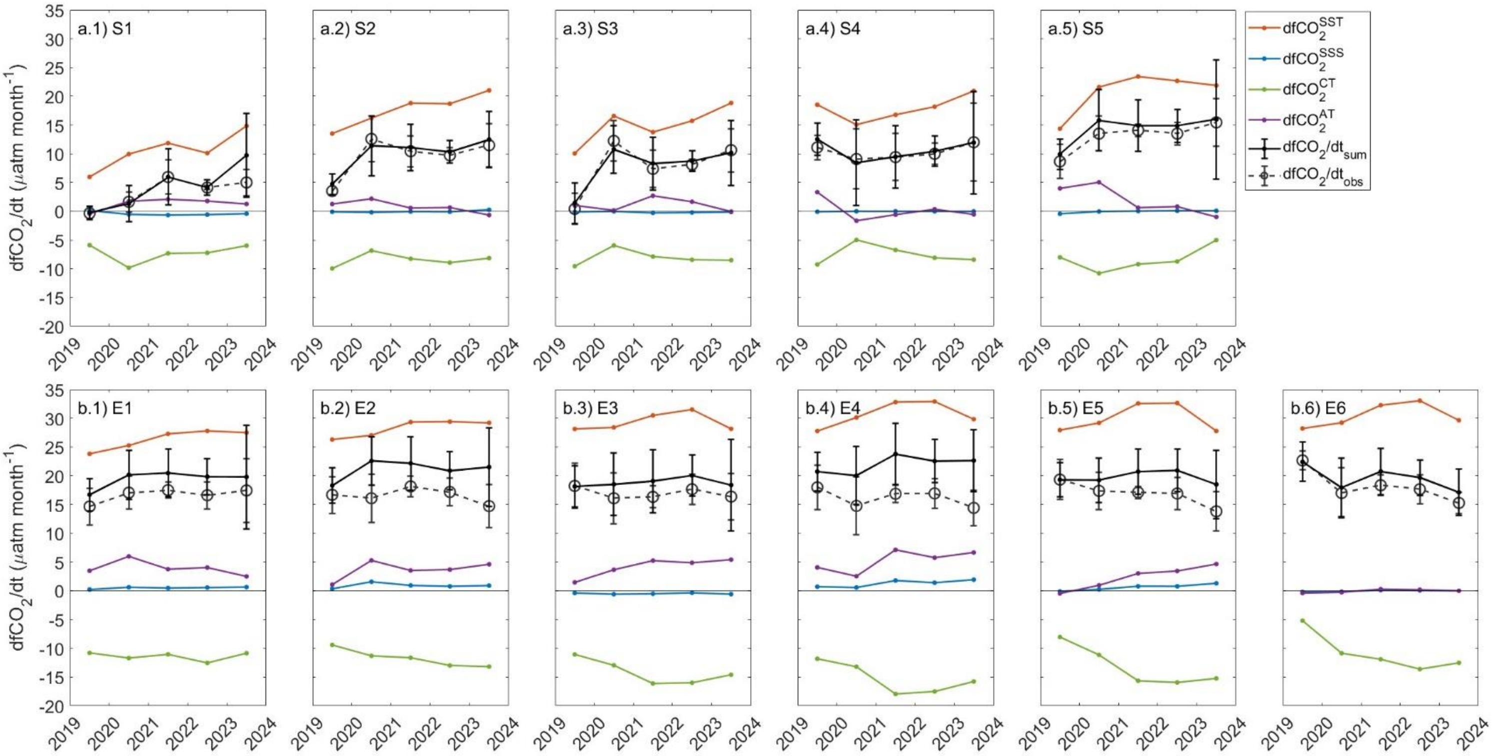

a.1) S1
a.2) S2
a.3) S3
a.4) S4
a.5) S5
b.1) E1
b.2) E2
b.3) E3
b.4) E4
b.5) E5
b.6) E6
$dfCO_2^{SST}$
$dfCO_2^{SSS}$
$dfCO_2^{CT}$
$dfCO_2^{AT}$
$dfCO_2/dt_{sum}$
$dfCO_2/dt_{obs}$
$dfCO_2/dt$ (μatm month^{-1})

Fig. 6

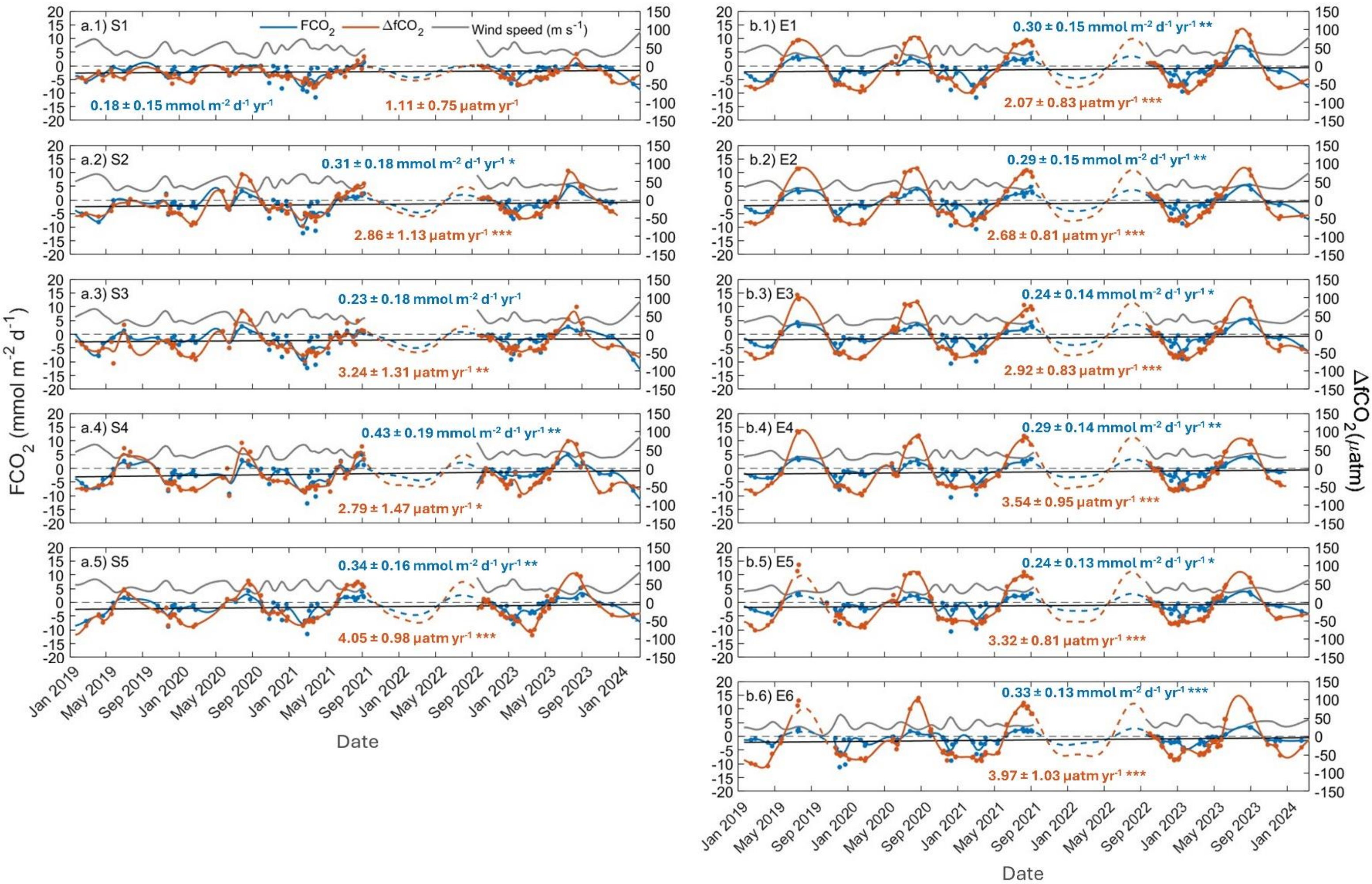

a.1) S1
FCO2
ΔfCO2
Wind speed (m s-1)
0.18 ± 0.15 mmol m-2 d-1 yr-1
1.11 ± 0.75 µatm yr-1
a.2) S2
0.31 ± 0.18 mmol m-2 d-1 yr-1 *
2.86 ± 1.13 µatm yr-1 ***
a.3) S3
0.23 ± 0.18 mmol m-2 d-1 yr-1
3.24 ± 1.31 µatm yr-1 **
a.4) S4
0.43 ± 0.19 mmol m-2 d-1 yr-1 **
2.79 ± 1.47 µatm yr-1 *
a.5) S5
0.34 ± 0.16 mmol m-2 d-1 yr-1 **
4.05 ± 0.98 µatm yr-1 ***
b.1) E1
0.30 ± 0.15 mmol m-2 d-1 yr-1 **
2.07 ± 0.83 µatm yr-1 ***
b.2) E2
0.29 ± 0.15 mmol m-2 d-1 yr-1 **
2.68 ± 0.81 µatm yr-1 ***
b.3) E3
0.24 ± 0.14 mmol m-2 d-1 yr-1 *
2.92 ± 0.83 µatm yr-1 ***
b.4) E4
0.29 ± 0.14 mmol m-2 d-1 yr-1 **
3.54 ± 0.95 µatm yr-1 ***
b.5) E5
0.24 ± 0.13 mmol m-2 d-1 yr-1 *
3.32 ± 0.81 µatm yr-1 ***
b.6) E6
0.33 ± 0.13 mmol m-2 d-1 yr-1 ***
3.97 ± 1.03 µatm yr-1 ***
FCO2 (mmol m-2 d-1)
ΔfCO2 (µatm)
Jan 2019
May 2019
Sep 2019
Jan 2020
May 2020
Sep 2020
Jan 2021
May 2021
Sep 2021
Jan 2022
May 2022
Sep 2022
Jan 2023
May 2023
Sep 2023
Jan 2024
Date

Fig. 7

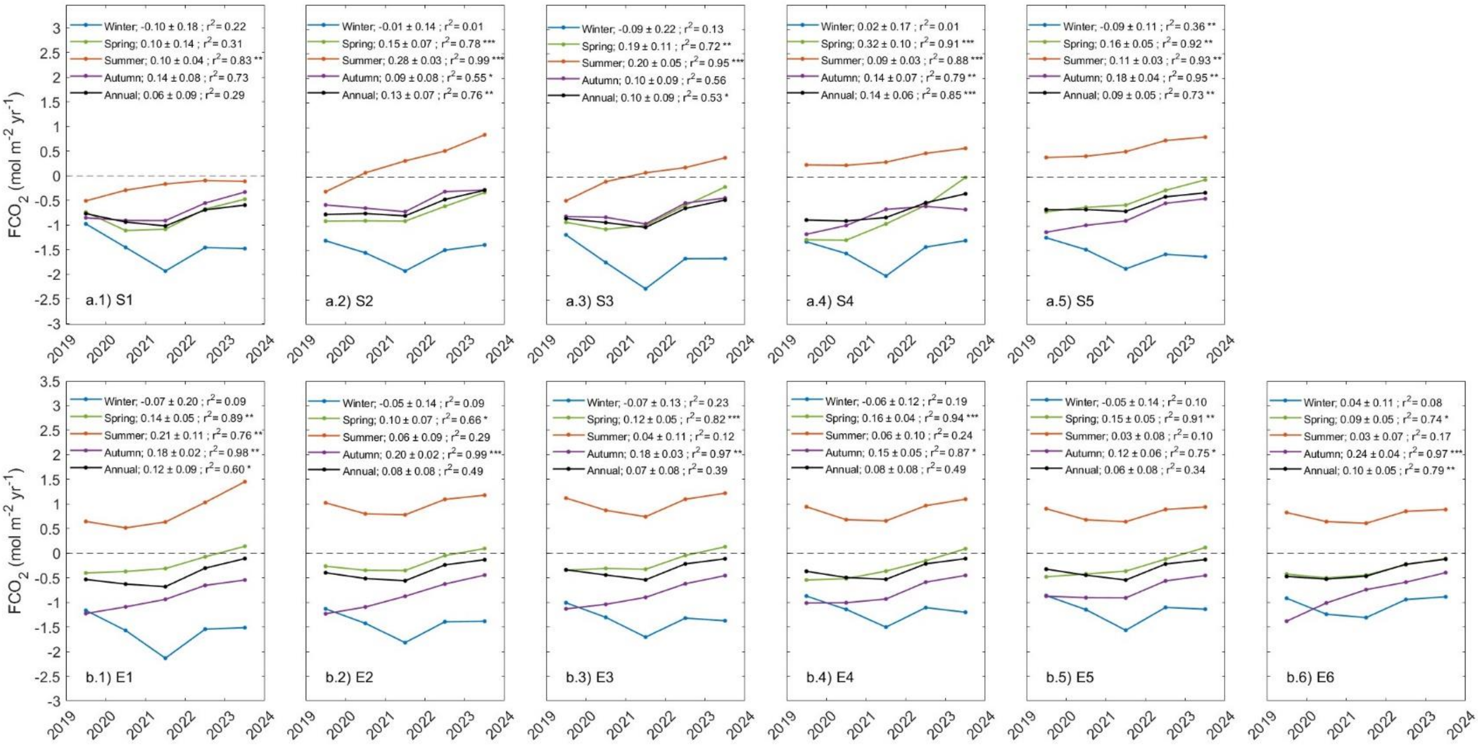

Winter; -0.10 ± 0.18 ; r2 = 0.22
Spring; 0.10 ± 0.14 ; r2 = 0.31
Summer; 0.10 ± 0.04 ; r2 = 0.83 **
Autumn; 0.14 ± 0.08 ; r2 = 0.73
Annual; 0.06 ± 0.09 ; r2 = 0.29
a.1) S1
Winter; -0.01 ± 0.14 ; r2 = 0.01
Spring; 0.15 ± 0.07 ; r2 = 0.78 ***
Summer; 0.28 ± 0.03 ; r2 = 0.99 ***
Autumn; 0.09 ± 0.08 ; r2 = 0.55 *
Annual; 0.13 ± 0.07 ; r2 = 0.76 **
a.2) S2
Winter; -0.09 ± 0.22 ; r2 = 0.13
Spring; 0.19 ± 0.11 ; r2 = 0.72 **
Summer; 0.20 ± 0.05 ; r2 = 0.95 ***
Autumn; 0.10 ± 0.09 ; r2 = 0.56
Annual; 0.10 ± 0.09 ; r2 = 0.53 *
a.3) S3
Winter; 0.02 ± 0.17 ; r2 = 0.01
Spring; 0.32 ± 0.10 ; r2 = 0.91 ***
Summer; 0.09 ± 0.03 ; r2 = 0.88 ***
Autumn; 0.14 ± 0.07 ; r2 = 0.79 **
Annual; 0.14 ± 0.06 ; r2 = 0.85 ***
a.4) S4
Winter; -0.09 ± 0.11 ; r2 = 0.36 **
Spring; 0.16 ± 0.05 ; r2 = 0.92 **
Summer; 0.11 ± 0.03 ; r2 = 0.93 **
Autumn; 0.18 ± 0.04 ; r2 = 0.95 **
Annual; 0.09 ± 0.05 ; r2 = 0.73 **
a.5) S5
Winter; -0.07 ± 0.20 ; r2 = 0.09
Spring; 0.14 ± 0.05 ; r2 = 0.89 **
Summer; 0.21 ± 0.11 ; r2 = 0.76 **
Autumn; 0.18 ± 0.02 ; r2 = 0.98 **
Annual; 0.12 ± 0.09 ; r2 = 0.60 *
b.1) E1
Winter; -0.05 ± 0.14 ; r2 = 0.09
Spring; 0.10 ± 0.07 ; r2 = 0.66 *
Summer; 0.06 ± 0.09 ; r2 = 0.29
Autumn; 0.20 ± 0.02 ; r2 = 0.99 ***
Annual; 0.08 ± 0.08 ; r2 = 0.49
b.2) E2
Winter; -0.07 ± 0.13 ; r2 = 0.23
Spring; 0.12 ± 0.05 ; r2 = 0.82 ***
Summer; 0.04 ± 0.11 ; r2 = 0.12
Autumn; 0.18 ± 0.03 ; r2 = 0.97 **
Annual; 0.07 ± 0.08 ; r2 = 0.39
b.3) E3
Winter; -0.06 ± 0.12 ; r2 = 0.19
Spring; 0.16 ± 0.04 ; r2 = 0.94 ***
Summer; 0.06 ± 0.10 ; r2 = 0.24
Autumn; 0.15 ± 0.05 ; r2 = 0.87 *
Annual; 0.08 ± 0.08 ; r2 = 0.49
b.4) E4
Winter; -0.05 ± 0.14 ; r2 = 0.10
Spring; 0.15 ± 0.05 ; r2 = 0.91 **
Summer; 0.03 ± 0.08 ; r2 = 0.10
Autumn; 0.12 ± 0.06 ; r2 = 0.75 *
Annual; 0.06 ± 0.08 ; r2 = 0.34
b.5) E5
Winter; 0.04 ± 0.11 ; r2 = 0.08
Spring; 0.09 ± 0.05 ; r2 = 0.74 *
Summer; 0.03 ± 0.07 ; r2 = 0.17
Autumn; 0.24 ± 0.04 ; r2 = 0.97 ***
Annual; 0.10 ± 0.05 ; r2 = 0.79 **
b.6) E6
FCO2 (mol m-2 yr-1)
2019
2020
2021
2022
2023
2024

Table 1

	SST		SSS		$fCO_{2,sw}$		pH		pH_{19}		C_T		NC_T		A_T		NA_T	
	Seasonal amplitude (°C)	Trend (°C yr^{-1})	Seasonal amplitude	Trend (°C yr^{-1})	Seasonal amplitude (μatm)	Trend (°C yr^{-1})	Seasonal amplitude (total scale)	Trend (°C yr^{-1})	Seasonal amplitude (total scale)	Trend (°C yr^{-1})	Seasonal amplitude (μmol kg^{-1})	Trend (°C yr^{-1})	Seasonal amplitude (μmol kg^{-1})	Trend (°C yr^{-1})	Seasonal amplitude (μmol kg^{-1})	Trend (°C yr^{-1})	Seasonal amplitude (μmol kg^{-1})	Trend (°C yr^{-1})
S1	4.21 ± 1.90	0.28 ± 0.07 ***	0.293 ± 0.328	-0.074 ± 0.012 ***	27.78 ± 20.27	3.13 ± 0.75 ***	0.0300 ± 0.0210	-0.0040 ± 0.0008 ***	0.0344 ± 0.0280	0.0002 ± 0.0010	41.2 ± 16.3	-6.4 ± 1.0 ***	26.8 ± 16.3	-2.2 ± 0.6 ***	29.4 ± 32.8	-7.4 ± 1.2 ***	10.6 ± 5.9	-2.7 ± 0.4 ***
S2	7.50 ± 2.18	0.50 ± 0.09 ***	0.158 ± 0.258	-0.078 ± 0.010 ***	70.20 ± 28.27	4.68 ± 1.10 ***	0.0674 ± 0.0254	-0.0055 ± 0.0010 ***	0.0582 ± 0.0292	0.0022 ± 0.0011 *	37.3 ± 19.4	-7.9 ± 1.1 ***	35.4 ± 19.4	-3.5 ± 0.8 ***	15.6 ± 25.9	-7.9 ± 1.0 ***	5.6 ± 4.7	-2.9 ± 0.4 ***
S3	6.42 ± 2.38	0.36 ± 0.09 ***	0.333 ± 0.334	-0.070 ± 0.012 ***	57.23 ± 35.36	5.12 ± 1.32 ***	0.0563 ± 0.0340	-0.0059 ± 0.0013 ***	0.0455 ± 0.0276	-0.0004 ± 0.0010	47.4 ± 17.6	-5.7 ± 1.1 ***	33.0 ± 17.6	-1.8 ± 0.7 ***	33.4 ± 33.7	-7.0 ± 1.3 ***	12.1 ± 6.1	-2.6 ± 0.5 ***
S4	7.53 ± 2.58	0.26 ± 0.10 ***	0.344 ± 0.457	-0.051 ± 0.017 ***	74.89 ± 38.91	4.89 ± 1.45 ***	0.0698 ± 0.0372	-0.0053 ± 0.0014 ***	0.0544 ± 0.0242	-0.0014 ± 0.0009	43.0 ± 19.9	-3.6 ± 1.6 ***	33.0 ± 19.9	-0.6 ± 0.7	34.7 ± 46.3	-5.2 ± 1.7 ***	12.5 ± 8.2	-1.9 ± 0.6 ***
S5	9.25 ± 2.34	0.45 ± 0.09 ***	0.562 ± 0.575	-0.062 ± 0.022 ***	96.99 ± 25.18	6.17 ± 0.98 ***	0.0940 ± 0.0242	-0.0067 ± 0.0009 ***	0.0601 ± 0.0304	0.0003 ± 0.0012	50.8 ± 24.3	-5.6 ± 2.0 ***	34.3 ± 24.3	-2.0 ± 0.9 ***	56.6 ± 58.0	-6.3 ± 2.2 ***	20.1 ± 10.3	-2.3 ± 0.8 ***
summer		0.59 ± 0.20 ***		-0.031 ± 0.021		7.23 ± 2.33 ***		-0.0069 ± 0.0020 ***		0.0020 ± 0.0014		-3.9 ± 1.4 ***		-2.1 ± 0.7 ***		-3.1 ± 2.2		-1.1 ± 0.8
winter		0.26 ± 0.04 ***		-0.094 ± 0.020 ***		3.43 ± 0.96 ***		-0.0047 ± 0.0011 ***		-0.0006 ± 0.0010		-7.8 ± 1.8 ***		-2.4 ± 0.8 ***		-9.5 ± 2.0 ***		-3.4 ± 0.7 ***
total		0.38 ± 0.05 ***		-0.065 ± 0.009 ***		4.76 ± 0.59 ***		-0.0054 ± 0.0006 ***		0.0002 ± 0.0005		-5.7 ± 0.8 ***		-2.0 ± 0.4 ***		-6.6 ± 0.9 ***		-2.4 ± 0.3 ***
2000-2019		0.03 ± 0.00 ***																
E1	11.07 ± 2.15	0.28 ± 0.08 ***	0.522 ± 0.463	-0.069 ± 0.017 ***	116.94 ± 23.18	4.44 ± 0.85 ***	0.1148 ± 0.0234	-0.0052 ± 0.0009 ***	0.0670 ± 0.0206	-0.0008 ± 0.0008	81.1 ± 15.1	-5.5 ± 1.4 ***	52.6 ± 15.1	-1.5 ± 0.6 ***	52.7 ± 47.0	-7.0 ± 1.7 ***	18.3 ± 8.2	-2.4 ± 0.6 ***
E2	11.64 ± 1.82	0.31 ± 0.07 ***	0.482 ± 0.486	-0.094 ± 0.018 ***	121.57 ± 21.54	4.79 ± 0.81 ***	0.1172 ± 0.0218	-0.0059 ± 0.0008 ***	0.0732 ± 0.0190	-0.0011 ± 0.0007	83.2 ± 13.5	-7.4 ± 1.5 ***	56.8 ± 13.5	-1.9 ± 0.5 ***	48.8 ± 49.2	-9.5 ± 1.9 ***	16.9 ± 8.5	-3.3 ± 0.6 ***
E3	12.44 ± 1.89	0.24 ± 0.07 ***	0.592 ± 0.604	-0.138 ± 0.023 ***	124.78 ± 21.85	4.99 ± 0.82 ***	0.1225 ± 0.0204	-0.0067 ± 0.0008 ***	0.0818 ± 0.0236	-0.0031 ± 0.0009 ***	94.1 ± 21.4	-10.2 ± 2.0 ***	63.9 ± 21.4	-2.0 ± 0.8 ***	60.0 ± 61.2	-14.0 ± 2.3 ***	20.6 ± 10.5	-4.8 ± 0.8 ***
E4	13.04 ± 1.80	0.23 ± 0.07 ***	0.768 ± 0.493	-0.068 ± 0.018 ***	120.73 ± 25.43	5.40 ± 0.94 ***	0.1196 ± 0.0234	-0.0061 ± 0.0009 ***	0.0891 ± 0.0280	-0.0024 ± 0.0010 **	120.1 ± 21.6	-4.4 ± 1.7 ***	75.1 ± 21.6	-0.4 ± 0.8	77.9 ± 49.9	-6.9 ± 1.8 ***	26.5 ± 8.5	-2.3 ± 0.6 ***
E5	12.92 ± 1.74	0.23 ± 0.06 ***	0.538 ± 0.467	-0.097 ± 0.017 ***	118.88 ± 21.72	5.31 ± 0.79 ***	0.1165 ± 0.0194	-0.0064 ± 0.0007 ***	0.0914 ± 0.0270	-0.0029 ± 0.0010 ***	98.4 ± 20.8	-6.6 ± 1.6 ***	69.3 ± 20.8	-0.9 ± 0.7	54.6 ± 47.3	-9.9 ± 1.7 ***	18.5 ± 8.0	-3.3 ± 0.6 ***
E6	13.13 ± 2.02	0.19 ± 0.07 ***	0.108 ± 0.551	-0.011 ± 0.015	124.68 ± 30.17	6.09 ± 0.99 ***	0.1159 ± 0.0256	-0.0061 ± 0.0008 ***	0.0929 ± 0.0328	-0.0032 ± 0.0011 ***	63.3 ± 27.4	0.9 ± 1.6	59.3 ± 27.4	1.6 ± 0.9	10.0 ± 54.7	-1.2 ± 1.4	3.4 ± 9.2	-0.4 ± 0.5
summer		0.29 ± 0.09 ***		-0.069 ± 0.042 *		-2.30 ± 1.02 **		0.0011 ± 0.0008		0.0037 ± 0.0012 ***		-8.5 ± 3.2 ***		-4.3 ± 0.9 ***	±	-7.0 ± 4.3	±	-2.4 ± 1.5
winter		0.20 ± 0.04 ***		-0.092 ± 0.023 ***		5.44 ± 0.41 ***		-0.0067 ± 0.0005 ***		-0.0036 ± 0.0007 ***		-5.8 ± 2.1 ***		-0.4 ± 0.8	±	-9.4 ± 2.4 ***	±	-3.2 ± 0.8 ***
total		0.30 ± 0.04 ***		-0.082 ± 0.013 ***		5.16 ± 0.37 ***		-0.0061 ± 0.0004 ***		-0.0022 ± 0.0004 ***		-5.8 ± 1.1 ***		-0.9 ± 0.4 ***	±	-8.4 ± 1.3 ***	±	-2.9 ± 0.4 ***
2000-2019		0.05 ± 0.01 ***																

Table 2

	$fCO_{2,sw}$ (thermal)						$fCO_{2,sw}$ (non-thermal)						T/B ratio	
	T'02			F'22			T'02			F'22				
	Mean (µatm)	Seasonal Amplitude (µatm)	Trend (µatm yr^{-1})	Mean (µatm)	Seasonal Amplitude (µatm)	Trend (µatm yr^{-1})	Mean (µatm)	Seasonal Amplitude (µatm)	Trend (µatm yr^{-1})	Mean (µatm)	Seasonal Amplitude (µatm)	Trend (µatm yr^{-1})	T'02	F'22
S1		70.35 ± 16.39	4.53 ± 1.21 ***		68.40 ± 15.85	4.42 ± 1.17 ***		41.04 ± 14.67	-1.53 ± 1.08		41.44 ± 14.70	-1.35 ± 1.09	1.71	1.65
S2		129.76 ± 19.66	8.50 ± 1.53 ***		124.45 ± 18.69	8.18 ± 1.46 ***		66.85 ± 17.44	-3.83 ± 1.36 ***		67.53 ± 15.90	-3.50 ± 1.24 ***	1.94	1.84
S3	392.04 ± 40.87	109.35 ± 21.50	6.04 ± 1.60 ***	389.02 ± 39.15	104.93 ± 20.41	5.80 ± 1.52 ***	386.13 ± 18.44	54.11 ± 15.14	-0.79 ± 1.13	386.62 ± 18.77	54.02 ± 14.31	-0.68 ± 1.06	2.02	1.94
S4		131.09 ± 23.60	4.36 ± 1.76 **		125.63 ± 22.41	4.19 ± 1.67 ***		59.99 ± 14.14	0.82 ± 1.05		61.82 ± 13.68	0.74 ± 1.02	2.19	2.03
S5		163.37 ± 20.70	7.79 ± 1.61 ***		154.95 ± 19.60	7.43 ± 1.52 ***		65.16 ± 17.94	-1.31 ± 1.39		68.85 ± 16.76	-1.25 ± 1.30	2.51	2.25
summer			11.83 ± 3.68 ***			11.09 ± 3.39 ***			-2.92 ± 1.23 **			-3.94 ± 1.44 ***		
winter			3.97 ± 0.70 ***			3.81 ± 0.74 ***			-0.62 ± 1.16			-0.29 ± 1.03		
total			6.20 ± 0.81 ***			5.94 ± 0.77 ***			-1.27 ± 0.57 **			-1.14 ± 0.55 **		
E1		196.07 ± 19.09	5.11 ± 1.40 ***		186.41 ± 18.12	4.84 ± 1.32 ***		81.74 ± 10.92	-0.18 ± 0.80		83.96 ± 10.83	-0.53 ± 0.79	2.40	2.22
E2		206.32 ± 16.29	5.29 ± 1.23 ***		196.92 ± 15.51	5.09 ± 1.17 ***		89.84 ± 9.73	-0.07 ± 0.73		91.97 ± 9.61	-0.32 ± 0.72	2.30	2.14
E3	400.22 ± 70.68	219.12 ± 16.15	3.86 ± 1.20 ***	399.02 ± 67.76	213.60 ± 15.79	3.80 ± 1.17 ***	389.61 ± 32.15	99.59 ± 13.95	1.43 ± 1.03	385.00 ± 33.52	105.81 ± 13.10	1.21 ± 0.97	2.20	2.02
E4		230.66 ± 15.37	3.75 ± 1.13 ***		222.49 ± 14.90	3.68 ± 1.10 ***		110.60 ± 15.39	1.58 ± 1.13		116.16 ± 15.56	1.67 ± 1.15	2.09	1.92
E5		229.35 ± 14.52	3.64 ± 1.05 ***		219.99 ± 14.06	3.55 ± 1.01 ***		108.60 ± 15.35	1.93 ± 1.11 *		115.03 ± 14.74	1.72 ± 1.06	2.11	1.91
E6		231.16 ± 17.30	2.88 ± 1.28 **		221.64 ± 16.61	2.84 ± 1.23 **		104.92 ± 19.24	3.37 ± 1.33 ***		109.10 ± 18.90	3.25 ± 1.29 ***	2.20	2.03
summer			6.41 2.13 ***			5.85 2.07 ***			-4.79 1.12 ***			-6.62 1.63 ***		
winter			2.78 0.60 ***			2.77 0.59 ***			2.91 0.83 ***			2.62 0.67 ***		
total			4.10 0.52 ***			3.95 0.51 ***			1.33 0.46 ***			1.19 0.47 ***		

References

Alberola, C., Millot, C., and Font, J.: On the seasonal and mesoscale variabilities of the Northern Current during the PRIMO-0 experiment in the western Mediterranean Sea, Oceanol. Acta, 18, 163–192, 1995.

Álvarez, M., Sanleón-Bartolomé, H., Tanhua, T., Mintrop, L., Luchetta, A., Cantoni, C., Schroeder, K., and Civitarese, G.: The CO2 system in the Mediterranean Sea: a basin-wide perspective, Ocean Sci., 10, 69–92, https://doi.org/10.5194/os-10-69-2014, 2014.

Antoine, D., Chami, M., Claustre, H., d'Ortenzio, F., Morel, A., Bécu, G., Gentili, B., Louis, F., Ras, J., Roussier, E., Scott, A. J., Tailliez, D., Hooker, S. B., Guevel, P., Desté, J. F., Dempsey, C., and Adams, D.: BOUSSOLE: A joint CNRS-INSU, ESA, CNES, and NASA ocean color calibration and validation activity, NASA Tech. Memo., 1–59, 2006.

Antoine, D., d'Ortenzio, F., Hooker, S. B., Bécu, G., Gentili, B., and Tailliez, D., Scott, A. J.: Assessment of uncertainty in the ocean reflectance determined by three satellite ocean color sensors (MERIS, SeaWiFS and MODIS-A) at an offshore site in the Mediterranean Sea (BOUSSOLE project), J. Geophys. Res. Ocean., 113, https://doi.org/10.1029/2007JC004472, 2008a.

Antoine, D., Guevel, P., Desté, J. F., Bécu, G., Louis, F., Scott, A. J., and Bardey, P.: The "BOUSSOLE" Buoy - A new transparent-to-swell taut mooring dedicated to marine optics: Design, tests, and performance at sea, J. Atmos. Ocean. Technol., 25, 968–989, https://doi.org/10.1175/2007JTECHO563.1, 2008b.

Bakker, D. C. E., Alin, S. R., Bates, N., Becker, M., Gkritzalis, T., Jones, S. D., Kozyr, A., Lauvset, S. K., Metzl, N., Nakaoka, S., O'Brien, K. M., Olsen, A., Pierrot, D., Steinhoff, T., Sutton, A. J., Takao, S., Tilbrook, B., Wada, C., Wanninkhof, R., Akl, J., Arbilla, L. A., Arruda, R., Azetsu-Scott, K., Barbero, L., Beatty, C. M., Berghoff, C. F., Bittig, H. C., Burger, E. F., Campbell, K., Cardin, V., Collins, A., Coppola, L., Cronin, M., Cross, J. N., Currie, K. I., Emerson, S. R., Enright, M. P., Enyo, K., Evans, W., Feely, R. A., Flohr, A., Gehrung, M., Glockzin, M., González-Dávila, M., Hamnca, S., Hartman, S., Howden, S. D., Kam, K., Kamb, L., Körtzinger, A., Kosugi, N., Lefèvre, N., Lo Monaco, C., Macovei, V. A., Maenner Jones, S., Manalang, D., Martz, T. R., Mdokwana, B., Monacci, N. M., Monteiro, P. M. S., Mordy, C., Morell, J. M., Murata, A., Neill, C., Noh, J.-H., Nojiri, Y., Ohman, M. D., Olivier, L., Ono, T., Petersen, W., Plueddemann, A. J., Prytherch, J., Rehder, G., Rutgersson, A., Santana-Casiano, J. M., Schlitzer, R., Send, U., Skjelvan, I., Sullivan, K. F., T'Jampens, M., Tadokoro, K., Telszewski, M., Theetaert, H., Tsanwani, M., Vandemark, D., van Ooijen, E., Veccia, M. H., Voynova, Y. G., Wang, H., Weller, R. A., and Woosley, R. J.: Surface Ocean CO2 Atlas Database Version 2024 (SOCATv2024), NOAA Natl. Centers for Environ. Inf., Dataset, https://doi.org/10.25921/9wpn-th28, Accessed: 15 May 2025, 2024.

Bakker, D. C. E., Pfeil, B., Landa, C. S., Metzl, N., O'Brien, K. M., Olsen, A., Smith, K., Cosca, C., Harasawa, S., Jones, S. D., Nakaoka, S., Nojiri, Y., Schuster, U., Steinhoff, T., Sweeney, C., Takahashi, T., Tilbrook, B., Wada, C., Wanninkhof, R., Alin, S. R., Balestrini, C. F., Barbero, L., Bates, N. R., Bianchi, A. A., Bonou, F., Boutin, J., Bozec, Y., Burger, E. F., Cai, W.-J., Castle, R. D., Chen, L., Chierici, M., Currie, K., Evans, W., Featherstone, C., Feely, R. A., Fransson, A., Goyet, C., Greenwood, N., Gregor, L., Hankin, S., Hardman-Mountford, N. J., Harlay, J., Hauck, J., Hoppema, M., Humphreys, M. P., Hunt, C. W., Huss, B., Ibánhez, J. S. P., Johannessen, T., Keeling, R., Kitidis, V., Körtzinger, A., Kozyr, A., Krasakopoulou, E., Kuwata, A., Landschützer, P., Lauvset, S. K., Lefèvre, N., Lo Monaco, C., Manke, A., Mathis, J. T., Merlivat, L., Millero, F. J., Monteiro, P. M. S., Munro, D. R., Murata, A., Newberger, T., Omar, A. M., Ono, T., Paterson, K., Pearce, D., Pierrot, D., Robbins, L. L., Saito, S., Salisbury, J., Schlitzer, R., Schneider, B., Schweitzer, R., Sieger, R., Skjelvan, I., Sullivan, K. F., Sutherland, S. C., Sutton, A. J., Tadokoro, K., Telszewski, M., Tuma, M., Van Heuven, S. M. A. C., Vandemark, D., Ward, B., Watson, A. J., and Xu, S.: A multi-decade record of high quality fCO2 data in version 3 of the Surface Ocean CO2 Atlas (SOCAT), Earth Syst. Sci. Data, 8, 383–413, https://doi.org/10.5194/essd-8-383-2016, 2016.

Bates, N. R., Astor, Y. M., Church, M. J., Currie, K., Dore, J. E., González-Dávila, M., Lorenzoni, L., Muller-Karger, F., Olafsson, J., and Santana-Casiano, J. M.: A time-series view of changing surface ocean chemistry due to ocean uptake of anthropogenic CO2 and ocean acidification, Oceanography, 27, 126–141, https://doi.org/10.5670/oceanog.2014.16, 2014.

Bégovic, M., and Copin-Montégut, C.: Processes controlling annual variations in the partial pressure of CO2 in surface waters of the central northwestern Mediterranean Sea

(Dyfamed site), Deep Sea Res. Part II Top. Stud. Oceanogr., 49, 2031–2047, https://doi.org/10.1016/S0967-0645(02)00026-7, 2002.

Bergamasco, A., and Malanotte-Rizzoli, P.: The circulation of the Mediterranean Sea: a historical review of experimental investigations, Adv. Oceanogr. Limnol., 1, 11–28, https://doi.org/10.1080/19475721.2010.505354, 2010.

Bolado-Penagos, M., González, C. J., Chioua, J., Sala, I., Jesús Gomiz-Pascual, J., Vázquez, Á., and Bruno, M.: Submesoscale processes in the coastal margins of the Strait of Gibraltar. The Trafalgar – Alboran connection, Prog. Oceanogr., 181, 102219, https://doi.org/10.1016/j.pocean.2019.102219, 2020.

Borges, A. V., Delille, B., and Frankignoulle, M.: Budgeting sinks and sources of CO2 in the coastal ocean: Diversity of ecosystem counts, Geophys. Res. Lett., 32, 1–4, https://doi.org/10.1029/2005GL023053, 2005.

Borghini, M. B. H. S., Bryden, H., Schroeder, K., Sparnocchia, S., and Vetrano, A.: The Mediterranean is becoming saltier, Ocean Sci., 10, 693–700, https://doi.org/10.5194/os-10-693-2014, 2014.

Bormans, M., and Garrett, C.: A simple criterion for gyre formation by the surface outflow from a strait, with application to the Alboran Sea, J. Geophys. Res. Ocean., 94, 12,637–12,644, https://doi.org/10.1029/JC094iC09p12637, 1989.

Bosse, A., Testor, P., Damien, P., Estournel, C., Marsaleix, P., Mortier, L., Prieur, L., and Taillandier, V.: Wind-forced submesoscale symmetric instability around deep convection in the northwestern Mediterranean Sea, Fluids, 6, 1–26, https://doi.org/10.3390/fluids6030123, 2021.

Bourg, N., and Molcard, A.: Northern boundary current variability and mesoscale dynamics: a long-term HF RADAR monitoring in the North-Western Mediterranean Sea, Ocean Dyn., 71, 851–870, https://doi.org/10.1007/s10236-021-01466-9, 2021.

Bray, N. A., Ochoa, J., and Kinder, T. H.: The role of the interface in exchange through the Strait of Gibraltar, J. Geophys. Res., https://doi.org/10.1029/95JC00381, 1995.

Cai, W. J., Dai, M., and Wang, Y.: Air-sea exchange of carbon dioxide in ocean margins: A province-based synthesis, Geophys. Res. Lett., 33, https://doi.org/10.1029/2006GL026219, 2006.

Chen, C. T. A., Huang, T. H., Chen, Y. C., Bai, Y., He, X., and Kang, Y.: Air-sea exchanges of CO2 in the world's coastal seas, Biogeosciences, 10, 6509–6544, https://doi.org/10.5194/bg-10-6509-2013, 2013.

Conan, P., and Millot, C.: Variability of the northern current off Marseilles, western Mediterranean Sea, from February to June 1992, Oceanol. Acta, 18, 193–205, https://doi.org/10.1016/0399-1784(95)00009-Q, 1995.

Copin-Montégut, C.: Alkalinity and carbon budgets in the Mediterranean Sea, Global Biogeochem. Cycles, 7, 915–925, https://doi.org/10.1029/93GB01740, 1993.

Copin-Montégut, C., and Bégovic, M.: Distributions of carbonate properties and oxygen along the water column (0–2000 m) in the central part of the NW Mediterranean Sea (Dyfamed site): Influence of winter vertical mixing on air–sea CO2 and O2 exchanges, Deep Sea Res. Part II Top. Stud. Oceanogr., 49, 2049–2066, https://doi.org/10.1016/S0967-0645(02)00027-9, 2002.

Copin-Montégut, C., Bégovic, M., and Merlivat, L.: Variability of the partial pressure of CO2 on diel to annual time scales in the Northwestern Mediterranean Sea, Mar. Chem., 85, 169–189, https://doi.org/10.1016/j.marchem.2003.10.005, 2004.

Coppola, L., Boutin, J., Gattuso, J. P., Lefevre, D., and Metzl, N.: The Carbonate System in the Ligurian Sea, in: Mediterr. Sea Era Glob. Chang. 1 30 Years Multidiscip. Study Ligurian Sea, 79–103, https://doi.org/10.1002/9781119706960.CH4, 2020.

Cossarini, G., Feudale, L., Teruzzi, A., Bolzon, G., Coidessa, G., Solidoro, C., ... and Salon, S.: High-resolution reanalysis of the Mediterranean Sea biogeochemistry (1999–2019), Front. Mar. Sci., 8, 741486, https://doi.org/10.3389/fmars.2021.741486, 2021.

Cossarini, G., Lazzari, P., and Solidoro, C.: Spatiotemporal variability of alkalinity in the Mediterranean Sea, Biogeosciences, 12, 1647–1658, https://doi.org/10.5194/bg-12-1647-2015, 2015.

Curbelo-Hernández, D., González-Dávila, M., González, A. G., González-Santana, D., and Santana-Casiano, J. M.: CO2 fluxes in the Northeast Atlantic Ocean based on measurements from a surface ocean observation platform, Sci. Total Environ., 775, 145804, https://doi.org/10.1016/j.scitotenv.2021.145804, 2021a.

Curbelo-Hernández, D., González-Dávila, M., and Santana-Casiano, J. M.: The carbonate system and air-sea CO2 fluxes in coastal and open-ocean waters of the Macaronesia, Front. Mar. Sci., 10:1094250. https://doi.org/10.3389/fmars.2023.1094250, 2023.

Curbelo-Hernández, D., Pérez, F. F., González-Dávila, M., Gladyshev, S. V., González, A. G., González-Santana, D., Velo, A., Sokov, A., and Santana-Casiano, J. M.: Ocean Acidification trends and Carbonate System dynamics in the North Atlantic Subpolar Gyre during 2009–2019, EGUsphere [preprint], https://doi.org/10.5194/egusphere-2024-1388, 2024.

Curbelo-Hernández, D., Santana-Casiano, J. M., González, A. G., and González-Dávila, M.: Air-Sea CO2 Exchange in the Strait of Gibraltar, Front. Mar. Sci., 8, 1701, https://doi.org/10.3389/FMARS.2021.745304, 2021b.

De Carlo, E. H., Mousseau, L., Passafiume, O., and Drupp, P. S., and Gattuso, J. P.: Carbonate Chemistry and Air-Sea CO2 Flux in a NW Mediterranean Bay Over a Four-Year Period: 2007-2011, Aquat. Geochemistry, 19, 399–442, https://doi.org/10.1007/s10498-013-9217-4, 2013.

de la Paz, M., Gómez-Parra, A., and Forja, J.: Seasonal variability of surface fCO2 in the Strait of Gibraltar, Aquat. Sci., 71, 55–64, https://doi.org/10.1007/s00027-008-8060-y, 2009.

de la Paz, M., Huertas, E. M., Padín, X. A., González-Dávila, M., Santana-Casiano, J. M., Forja, J. M., Orbi, A., Pérez, F. F., and Ríos, A. F.: Reconstruction of the seasonal cycle of air-sea CO2 fluxes in the Strait of Gibraltar, Mar. Chem., 126, 155–162, https://doi.org/10.1016/j.marchem.2011.05.004, 2011.

Dickson, A. G.: Standard potential of the reaction: AgCl(s) + 1/2H2(g) = Ag(s) + HCl(aq), and the standard acidity constant of the ion HSO4- in synthetic sea water from 273.15 to

318.15 K, J. Chem. Thermodyn., 22, 113–127, https://doi.org/10.1016/0021-9614(90)90074-Z, 1990.

Dickson, A. G., and Goyet, C.: Handbook of methods for the analysis of the various parameters of the carbon dioxide system in sea water, Version 2, https://doi.org/10.2172/10107773, 1994.

Dickson, A. G., Sabine, C. L., and Chistian, J. R.: Guide to best practices for ocean CO2 measurements, PICES Special Publ. 3:191, 2007.

Dohan, K.: Journal of Geophysical Research: Oceans, J. Geophys. Res. Ocean., 122, 2647–2651, https://doi.org/10.1002/2016JC012144, 2017.

Doney, S. C., Fabry, V. J., Feely, R. A., and Kleypas, J. A.: Ocean Acidification: The Other CO2 Problem, Ann. Rev. Mar. Sci., 1, 169–192, https://doi.org/10.1146/annurev.marine.010908.163834, 2009.

D'Ortenzio, F., Antoine, D., and Marullo, S.: Satellite-driven modeling of the upper ocean mixed layer and air-sea CO2 flux in the Mediterranean Sea, Deep Sea Res. Part I Oceanogr. Res. Pap., 55, 405–434, https://doi.org/10.1016/j.dsr.2007.12.008, 2008.

Echevarría, F., García Lafuente, J., Bruno, M., Gorsky, G., Goutx, M., González, N., García, C. M., Gómez, F., Vargas, J. M., Picheral, M., Striby, L., Varela, M., Alonso, J. J., Reul, A., Cózar, A., Prieto, L., Sarhan, T., Plaza, F., and Jiménez-Gómez, F.: Physical-biological coupling in the Strait of Gibraltar, Deep Sea Res. Part II Top. Stud. Oceanogr., 49, 4115–4130, https://doi.org/10.1016/S0967-0645(02)00145-5, 2002.

Escudier, R., Clementi, E., Omar, M., Cipollone, A., Pistoia, J., Aydogdu, A., Drudi, M., Grandi, A., Lyubartsev, V., Lecci, R., Cretí, S., Masina, S., Coppini, G., and Pinardi, N.: Mediterranean Sea Physical Reanalysis (CMEMS MED-Currents) (Version 1) [Data set], Copernicus Monitoring Environment Marine Service (CMEMS), https://doi.org/10.25423/CMCC/MEDSEA_MULTIYEAR_PHY_006_004_E3R1, 2020.

Escudier, R., Clementi, E., Cipollone, A., Pistoia, J., Drudi, M., Grandi, A., Lyubartsev, V., Lecci, R., Aydogdu, A., Delrosso, D., Omar, M., Masina, S., Coppini, G., and Pinardi, N.: A High Resolution Reanalysis for the Mediterranean Sea, Front. Earth Sci., 9, 1060, https://doi.org/10.3389/feart.2021.702285, 2021.

Fassbender, A. J., Schlunegger, S., Rodgers, K. B., and Dunne, J. P.: Quantifying the Role of Seasonality in the Marine Carbon Cycle Feedback: An ESM2M Case Study, Global Biogeochem. Cycles, 36, 1–15, https://doi.org/10.1029/2021GB007018, 2022.

Folkard, A. M., Davies, P. A., Fiúza, A. F. G., and Ambar, I.: Remotely sensed sea surface thermal patterns in the Gulf of Cadiz and the Strait of Gibraltar: Variability, correlations, and relationships with the surface wind field, J. Geophys. Res. Ocean., 102, 5669–5683, https://doi.org/10.1029/96JC02505, 1997.

Ford, D. J., Tilstone, G. H., Shutler, J. D., and Kitidis, V.: Identifying the biological control of the annual and multi-year variations in South Atlantic air-sea CO2 flux, Biogeosciences, 19, 4287–4304, https://doi.org/10.5194/bg-19-4287-2022, 2022.

Frankignoulle, M., and Borges, A. V.: European continental shelf as a significant sink for atmospheric carbon dioxide, Global Biogeochem. Cycles, 15, 569–576, https://doi.org/10.1029/2000GB001307, 2001.

Friedlingstein, P., O'Sullivan, M., Jones, M. W., Andrew, R. M., Bakker, D. C. E., Hauck, J., Landschützer, P., Le Quéré, C., Luijkx, I. T., Peters, G. P., Peters, W., Pongratz, J., Schwingshackl, C., Sitch, S., Canadell, J. G., Ciais, P., Jackson, R. B., Alin, S. R., Anthoni, P., Barbero, L., Bates, N. R., Becker, M., Bellouin, N., Decharme, B., Bopp, L., Brasika, I. B. M., Cadule, P., Chamberlain, M. A., Chandra, N., Chau, T.-T.-T., Chevallier, F., Chini, L. P., Cronin, M., Dou, X., Enyo, K., Evans, W., Falk, S., Feely, R. A., Feng, L., Ford, D. J., Gasser, T., Ghattas, J., Gkritzalis, T., Grassi, G., Gregor, L., Gruber, N., Gürses, Ö., Harris, I., Hefner, M., Heinke, J., Houghton, R. A., Hurtt, G. C., Iida, Y., Ilyina, T., Jacobson, A. R., Jain, A., Jarníková, T., Jersild, A., Jiang, F., Jin, Z., Joos, F., Kato, E., Keeling, R. F., Kennedy, D., Klein Goldewijk, K., Knauer, J., Korsbakken, J. I., Körtzinger, A., Lan, X., Lefèvre, N., Li, H., Liu, J., Liu, Z., Ma, L., Marland, G., Mayot, N., McGuire, P. C., McKinley, G. A., Meyer, G., Morgan, E. J., Munro, D. R., Nakaoka, S.-I., Niwa, Y., O'Brien, K. M., Olsen, A., Omar, A. M., Ono, T., Paulsen, M., Pierrot, D., Pocock, K., Poulter, B., Powis, C. M., Rehder, G., Resplandy, L., Robertson, E., Rödenbeck, C., Rosan, T. M., Schwinger, J., Séférian, R., Smallman,

T. L., Smith, S. M., Sospedra-Alfonso, R., Sun, Q., Sutton, A. J., Sweeney, C., Takao, S., Tans, P. P., Tian, H., Tilbrook, B., Tsujino, H., Tubiello, F., van der Werf, G. R., van Ooijen, E., Wanninkhof, R., Watanabe, M., Wimart-Rousseau, C., Yang, D., Yang, X., Yuan, W., Yue, X., Zaehle, S., Zeng, J., and Zheng, B.: Global Carbon Budget 2023, Earth Syst. Sci. Data, 15, 5301–5369, https://doi.org/10.5194/essd-15-5301-2023, 2023.

Fröb, F., Olsen, A., Becker, M., Chafik, L., Johannessen, T., Reverdin, G., and Omar, A.: Wintertime fCO2 Variability in the Subpolar North Atlantic Since 2004, Geophys. Res. Lett., 46, 1580–1590, https://doi.org/10.1029/2018GL080554, 2019.

Frölicher, T. L., Fischer, E. M., and Gruber, N.: Marine heatwaves under global warming, Nature, 560, 360–364, https://doi.org/10.1038/s41586-018-0383-9, 2018.

García-Ibáñez, M. I., Zunino, P., Fröb, F., Carracedo, L. I., Ríos, A. F., Mercier, H., Olsen, A., and Pérez, F. F.: Ocean acidification in the subpolar North Atlantic: Rates and mechanisms controlling pH changes, Biogeosciences, 13, 3701–3715, https://doi.org/10.5194/bg-13-3701-2016, 2016.

García Lafuente, J., Álvarez Fanjul, E., Vargas, J. M., and Ratsimandresy, A. W.: Subinertial variability in the flow through the Strait of Gibraltar, J. Geophys. Res. Ocean., 107, 1–9, https://doi.org/10.1029/2001jc001104, 2002.

Gómez-Jakobsen, F. J., Mercado, J. M., Cortés, D., and Yebra, L., Salles, S.: A first description of the summer upwelling off the Bay of Algeciras and its role in the northwestern Alboran Sea, Estuar. Coast. Shelf Sci., 225, 106230, https://doi.org/10.1016/j.ecss.2019.05.012, 2019.

González-Dávila, M., and Santana-Casiano, J. M.: Long-term trends of pH and inorganic carbon in the Eastern North Atlantic: the ESTOC site, Front. Mar. Sci., 10, 1–16, https://doi.org/10.3389/fmars.2023.1236214, 2023.

Hersbach, H., Bell, B., Berrisford, P., Biavati, G., Horányi, A., Muñoz Sabater, J., Nicolas, J., Peubey, C., Radu, R., Rozum, I., Schepers, D., Simmons, A., Soci, C., Dee, D., and Thépaut, J.-N.: ERA5 hourly data on single levels from 1940 to present, Copernicus Climate Change Service (C3S) Climate Data Store (CDS), https://doi.org/10.24381/cds.adbb2d47, 2023.

Hoegh-Guldberg, O., Cai, R., Poloczanska, E. S., Brewer, P. G., Sundby, S., Hilmi, K., Fabry, V. J., and Jung, S.: The Ocean, in: Climate Change 2014: Impacts, Adaptation, and Vulnerability. Part B: Regional Aspects, Contribution of Working Group II to the Fifth Assessment Report of the Intergovernmental Panel on Climate Change, edited by: V. R. Barros, C. B. Field, D. J. Dokken, M. D. Mastrandrea, K. J. Mach, T. E. Bilir, M. Chatterjee, K. L. Ebi, Y. O. Estrada, R. C. Genova, B. Girma, E. S. Kissel, A. N. Levy, S. MacCracken, P. R. Mastrandrea, and L. L. White, Cambridge Univ. Press, Cambridge, UK and New York, NY, USA, 1655–1731, 2014.

Hoegh-Guldberg, O., Jacob, D., Taylor, M., Bindi, M., Brown, S., Camilloni, I., Diedhiou, A., Djalante, R., Ebi, K. L., Engelbrecht, F., Guiot, J., Hijioka, Y., Mehrotra, S., Payne, A., S. I. Seneviratne, A. Thomas, R. Warren, and G. Zhou: Impacts of 1.5ºC Global Warming on Natural and Human Systems, in: Global Warming of 1.5°C: An IPCC Special Report on the Impacts of Global Warming of 1.5°C Above Pre-Industrial Levels and Related Global Greenhouse Gas Emission Pathways, edited by: V. Masson-Delmotte, P. Zhai, H.-O. Pörtner, D. Roberts, J. Skea, P. R. Shukla, A. Pirani, W. Moufouma-Okia, C. Péan, R. Pidcock, S. Connors, J. B. R. Matthews, Y. Chen, X. Zhou, M. I. Gomis, E. Lonnoy, T. Maycock, M. Tignor, and T. Waterfield, Cambridge Univ. Press, Cambridge, UK and New York, NY, USA, 175–312, https://doi.org/10.1017/9781009157940.005, 2018.

Hood, E. M., and Merlivat, L.: Annual to interannual variations of fCO2 in the northwestern Mediterranean Sea: Results from hourly measurements made by CARIOCA buoys, 1995-1997, J. Mar. Res., 59, 113–131, https://doi.org/10.1357/002224001321237399, 2001.

IPCC: Climate Change 2023: Synthesis Report, Contribution of Working Groups I, II and III to the Sixth Assessment Report of the Intergovernmental Panel on Climate Change, edited by: H. Lee and J. Romero, IPCC, Geneva, Switzerland, 35–115, https://doi.org/10.59327/IPCC/AR6-9789291691647, 2023.

Jiang, Z. P., Tyrrell, T., Hydes, D. J., Dai, M., and Hartman, S. E.: Variability of alkalinity and the alkalinity–salinity relationship in the tropical and subtropical surface ocean, Global Biogeochem. Cycles, 28(7), 729–742, https://doi.org/10.1002/2013GB004678. 2014.

Johnson, K. M., Wills, K. D., Butler, D. B., Johnson, W. K., and Wong, C. S.: Coulometric total carbon dioxide analysis for marine studies: maximizing the performance of an automated gas extraction system and coulometric detector, Mar. Chem., 44, 167–187, https://doi.org/10.1016/0304-4203(93)90201-X, 1993.

Lacombe, H., and Richez, C.: The regime of the strait of Gibraltar, Elsevier Oceanogr. Ser., 34, 13–73, https://doi.org/10.1016/S0422-9894(08)71237-6, 1982.

Lee, K., Kim, T. W., Byrne, R. H., Millero, F. J., Feely, R. A., and Liu, Y. M.: The universal ratio of boron to chlorinity for the North Pacific and North Atlantic oceans, Geochim. Cosmochim. Acta, 74, 1801–1811, https://doi.org/10.1016/j.gca.2009.12.027, 2010.

Lee, K., Tong, L. T., Millero, F. J., Sabine, C. L., Dickson, A. G., Goyet, C., Park, G. H., Wanninkhof, R., Feely, R. A., and Key, R. M.: Global relationships of total alkalinity with salinity and temperature in surface waters of the world's oceans, Geophys. Res. Lett., 33, 1–5, https://doi.org/10.1029/2006GL027207, 2006.

Lewis, E., and Wallace, D.: Program Developed for CO2 System Calculations ORNL/CDIAC-105, Carbon Dioxide Information Analysis Centre, 1998.

López-García, M.J., Millot, C., Font, J., and García-Ladona, E.: Surface circulation variability in the Balearic Basin, J. Geophys. Res., 99, 3285–3296, https://doi.org/10.1029/93JC02114, 1994.

Lovenduski, N.S., Gruber, N., Doney, S.C., and Lima, I.D.: Enhanced CO2 outgassing in the Southern Ocean from a positive phase of the Southern Annular Mode, Global Biogeochem. Cycles, 21, 1–14, https://doi.org/10.1029/2006GB002900, 2007.

Lueker, T.J., Dickson, A.G., and Keeling, C.D.: Ocean pCO2 calculated from dissolved inorganic carbon, alkalinity, and equations for K1 and K2: Validation based on laboratory measurements of CO2 in gas and seawater at equilibrium, Mar. Chem., 70, 105–119, https://doi.org/10.1016/S0304-4203(00)00022-0, 2000.

Macías, D., Bruno, M., Echevarría, F., Vázquez, A., and García, C.M.: Meteorologically-induced mesoscale variability of the North-western Alboran Sea (southern Spain) and related biological patterns, Estuar. Coast. Shelf Sci., 78, 250–266, https://doi.org/10.1016/j.ecss.2007.12.008, 2008.

Macias, D., Garcia-Gorriz, E., and Stips, A.: The seasonal cycle of the Atlantic Jet dynamics in the Alboran Sea: Direct atmospheric forcing versus Mediterranean thermohaline circulation, Ocean Dyn., 66, 137–151, https://doi.org/10.1007/s10236-015-0914-y, 2016.

Marcellin Yao, K., Marcou, O., Goyet, C., Guglielmi, V., Touratier, F., and Savy, J.P.: Time variability of the north-western Mediterranean Sea pH over 1995–2011, Mar. Environ. Res., 116, 51–60, https://doi.org/10.1016/J.MARENVRES.2016.02.016, 2016.

Marty, J.C.: The DYFAMED time-series program (French-JGOFS), Deep-Sea Res. Part II Top. Stud. Oceanogr., 49, 1963–1964, https://doi.org/10.1016/S0967-0645(02)00021-8, 2002.

Mémery, L., Lévy, M., Vérant, S., and Merlivat, L.: The relevant time scales in estimating the air-sea CO2 exchange in a mid-latitude region, Deep-Sea Res. Part II Top. Stud. Oceanogr., 49, 2067–2092, https://doi.org/10.1016/S0967-0645(02)00028-0, 2002.

Merlivat, L., Boutin, J., Antoine, D., Beaumont, L., Golbol, M., and Vellucci, V.: Increase of dissolved inorganic carbon and decrease in pH in near-surface waters in the Mediterranean Sea during the past two decades, Biogeosciences, 15, 5653–5662, https://doi.org/10.5194/bg-15-5653-2018, 2018.

Millero, F.J., Zhang, J., Lee, K., and Campbell, D.M.: Titration alkalinity of seawater, Mar. Chem., 44, 153–165, https://doi.org/10.1016/0304-4203(93)90009-R, 1993.

Millero, F. J., Morse, J., and Chen, C. T.: The carbonate system in the western Mediterranean Sea, Deep-Sea Res. Part A Oceanogr. Res. Pap., 26, 1395–1404, https://doi.org/10.1016/0198-0149(79)90064-2, 1979.

Millot, C.: Circulation in the Western Mediterranean Sea, J. Mar. Syst., 20, 423–442, https://doi.org/10.1016/S0924-7963(98)00078-5, 1999.

Millot, C., and Taupier-Letage, I.: Circulation in the Mediterranean Sea, in: The Mediterranean Sea, edited by: S. G. The Mediterranean Sea, 29–66, 2005.

Minas, H.J., Coste, B., Le Corre, P., Minas, M., and Raimbault, P.: Biological and geochemical signatures associated with the water circulation through the Strait of Gibraltar and in the western Alboran Sea, J. Geophys. Res., 96, 8755–8771, https://doi.org/10.1029/91JC00360, 1991.

Mintrop, L., Pérez, F.F., González-Dávila, M., Santana-Casiano, J.M., and Körtzinger, A.: Alkalinity determination by potentiometry: Intercalibration using three different methods, Ciencias Mar., 26, 23–37, https://doi.org/10.7773/cm.v26i1.573, 2000.

Nielsen, J. N.: Hydrography of the Mediterranean and adjacent seas, Danish Oceanogr. Exped., 1908–10, Report I, 72–191, 1912.

Nigam, T., Escudier, R., Pistoia, J., Aydogdu, A., Omar, M., Clementi, E., Cipollone, A., Drudi, M., Grandi, A., Mariani, A., Lyubartsev, V., Lecci, R., Cretí, S., Masina, S., Coppini, G., and Pinardi, N.: Mediterranean Sea Physical Reanalysis INTERIM (CMEMS MED-Currents, E3R1i system) (Version 1) [Data set], Copernicus Monitoring Environment Marine Service (CMEMS), https://doi.org/10.25423/CMCC/MEDSEA_MULTIYEAR_PHY_006_004_E3R1I, 2021.

Oliver, E.C.J., Donat, M.G., Burrows, M.T., Moore, P.J., Smale, D.A., Alexander, L.V., Benthuysen, J.A., Feng, M., Sen Gupta, A., Hobday, A.J., Holbrook, N.J., Perkins-Kirkpatrick, S.E., Scannell, H.A., Straub, S.C., and Wernberg, T.: Longer and more frequent marine heatwaves over the past century, Nat. Commun., 9, 1–12, https://doi.org/10.1038/s41467-018-03732-9, 2018.

Orr, J. C., Epitalon, J.-M., Dickson, A. G., and Gattuso, J.-P.: Routine uncertainty propagation for the marine carbon dioxide system, Mar. Chem., 207, 84–107, https://doi.org/10.1016/j.marchem.2018.10.006, 2018.

Padin, X.A., Vazquez-Rodriguez, M., Castaño, M., Velo, A., Alonso-Perez, F., Gago, J., Gilcoto, M., Alvarez, M., Pardo, P.C., De La Paz, M., Rios, A.F., and Pérez, F.F.: Air-Sea CO2 fluxes in the Atlantic as measured during boreal spring and autumn, Biogeosciences, 7, 1587–1606, https://doi.org/10.5194/bg-7-1587-2010, 2010.

Palmiéri, J., Orr, J.C., Dutay, J.-C., Béranger, K., Schneider, A., Beuvier, J., and Somot, S.: Simulated anthropogenic CO2 storage and acidification of the Mediterranean Sea, Biogeosciences, 12, 781–802, https://doi.org/10.5194/bg-12-781-2015, 2015a.

Palmiéri, J., Orr, J.C., Dutay, J.C., Béranger, K., Schneider, A., Beuvier, J., and Somot, S.: Simulated anthropogenic CO2 storage and acidification of the Mediterranean Sea, Biogeosciences, 12, 781–802, https://doi.org/10.5194/bg-12-781-2015, 2015b.

Peliz, A., Boutov, D., and Teles-Machado, A.: The Alboran Sea mesoscale in a long term high resolution simulation: Statistical analysis, Ocean Model., 72, 32–52, https://doi.org/10.1016/j.ocemod.2013.07.002, 2013.

Peliz, Á., Teles-Machado, A., Marchesiello, P., Dubert, J., and Lafuente, J.G.: Filament generation off the Strait of Gibraltar in response to gap winds, Dyn. Atmos. Ocean., 46, 36–45, https://doi.org/10.1016/j.dynatmoce.2008.08.002, 2009.

Pérez, F.F., and Fraga, F.: Association constant of fluoride and hydrogen ions in seawater, Mar. Chem., 21, 161–168, https://doi.org/10.1016/0304-4203(87)90036-3, 1987.

Pérez, F.F., Olafsson, J., Ólafsdóttir, S.R., Fontela, M., and Takahashi, T.: Contrasting drivers and trends of ocean acidification in the subarctic Atlantic, Sci. Rep., 11, 1–16, https://doi.org/10.1038/s41598-021-93324-3, 2021.

Pierrot, D., Neill, C., Sullivan, K., Castle, R., Wanninkhof, R., Lüger, H., Johannessen, T., Olsen, A., Feely, R.A., and Cosca, C.E.: Recommendations for autonomous underway pCO2 measuring systems and data-reduction routines, Deep-Sea Res. Part II Top. Stud. Oceanogr., 56, 512–522, https://doi.org/10.1016/j.dsr2.2008.05.014, 2009.

Pinot, J. M., Tintoré, J., and Gomis, D.: Multivariate analysis of the surface circulation in the Balearic Sea, Prog. Oceanogr., 36, 343–376, https://doi.org/10.1016/0079-6611(96)00003-1, 1995.

Rayner, N. A., Parker, D. E., Horton, E. B., Folland, C. K., Alexander, L. V., Rowell, D. P., Kent, E. C., and Kaplan, A.: Global analyses of sea surface temperature, sea ice, and night marine air temperature since the late nineteenth century, J. Geophys. Res. Atmos., 108, https://doi.org/10.1029/2002jd002670, 2003.

Renault, L., Oguz, T., Pascual, A., Vizoso, G., and Tintore, J.: Surface circulation in the Alboran Sea (western Mediterranean) inferred from remotely sensed data, J. Geophys. Res. Ocean., 117, 1–11, https://doi.org/10.1029/2011JC007659, 2012.

Richez, C., and Kergomard, C.: Characteristic features occurring in the Strait of Gibraltar as seen through remote sensing data, Phys. Oceanogr. sea straits, 441–455, https://doi.org/10.1007/978-94-009-0677-8_21, 1990.

Rivaro, P., Messa, R., Massolo, S., and Frache, R.: Distributions of carbonate properties along the water column in the Mediterranean Sea: Spatial and temporal variations, Mar. Chem., 121, 236–245, https://doi.org/10.1016/j.marchem.2010.01.007, 2010.

Robinson, A. R., and Golnaraghi, M.: The physical and dynamical oceanography of the Mediterranean Sea, in: Ocean Processes in Climate Dynamics: Global and Mediterranean Examples, edited by: A. R. Robinson and K. Brink, 255–306, Dordrecht: Springer Netherlands, 1994.

Robinson, A. R., Leslie, W. G., Theocharis, A., and Lascaratos, A.: Mediterranean Sea circulation, Ocean Currents, 1, 19, 2001.

Rodgers, K. B., Schwinger, J., Fassbender, A. J., Landschützer, P., Yamaguchi, R., Frenzel, H., Stein, K., Müller, J. D., Goris, N., Sharma, S., Bushinsky, S., Chau, T. T. T., Gehlen, M., Gallego, M. A., Gloege, L., Gregor, L., Gruber, N., Hauck, J., Iida, Y., Ishii, M., Keppler, L., Kim, J. E., Schlunegger, S., Tjiputra, J., Toyama, K., Vaittinada Ayar, P., and Velo, A.: Seasonal Variability of the Surface Ocean Carbon Cycle: A Synthesis, Global Biogeochem. Cycles, 37, 1–34, https://doi.org/10.1029/2023GB007798, 2023.

Sammari, C., Millot, C., and Prieur, L.: Aspects of the seasonal and mesoscale variabilities of the Northern Current in the western Mediterranean Sea inferred from the PROLIG-2 and PROS-6 experiments, Deep-Sea Res. Part I, 42, 893–917, https://doi.org/10.1016/0967-0637(95)00031-Z, 1995.

Sánchez-Garrido, J. C., García Lafuente, J., Álvarez Fanjul, E., Sotillo, M. G., and de los Santos, F. J.: What does cause the collapse of the western Alboran gyre? Results of an operational ocean model, Prog. Oceanogr., 116, 142–153, https://doi.org/10.1016/j.pocean.2013.07.002, 2013.

Sánchez-Garrido, J. C., and Nadal, I.: The Alboran Sea circulation and its biological response: A review, Front. Mar. Sci., 9, 1–15, https://doi.org/10.3389/fmars.2022.933390, 2022.

Sarmiento, J., and Gruber, N.: Ocean Biogeochemical Dynamics, Princeton Univ. Press, Princeton, https://doi.org/10.1515/9781400849079, 2006.

Schneider, A., Tanhua, T., Körtzinger, A., and Wallace, D. W. R.: High anthropogenic carbon content in the eastern Mediterranean, J. Geophys. Res. Ocean., 115, 1–11, https://doi.org/10.1029/2010JC006171, 2010.

Schneider, A., Wallace, D. W., and Körtzinger, A.: Alkalinity of the Mediterranean Sea, Geophys. Res. Lett., 34(15), https://doi.org/10.1029/2006GL028842. 2007.

Schroeder, K., García-Lafuente, J., Josey, S. A., Artale, V., Nardelli, B. B., Carrillo, A., ... and Zodiatis, G.: Circulation of the Mediterranean Sea and its variability, in: The Climate of the Mediterranean Region, edited by: M. D. Alpert and L. O. Reinhold, 187, 2012.

Shadwick, E. H., Thomas, H., Comeau, A., Craig, S. E., Hunt, C. W., and Salisbury, J. E.: Air-Sea CO2 fluxes on the Scotian Shelf: Seasonal to multi-annual variability, Biogeosciences, 7, 3851–3867, https://doi.org/10.5194/bg-7-3851-2010, 2010.

Sharp, J. D., Pierrot, D., Humphreys, M. P., Epitalon, J.-M., Orr, J. C., Lewis, E. R., and Wallace, D. W. R.: CO2SYSv3 for MATLAB (Version v3.2.1), Zenodo, https://doi.org/10.5281/zenodo.3950562, 2023.

Sisma-Ventura, G., Bialik, O. M., Yam, R., Herut, B., and Silverman, J.: pCO2 variability in the surface waters of the ultra-oligotrophic Levantine Sea: Exploring the air–sea CO2 fluxes in a fast warming region, Mar. Chem., 196, 13–23, https://doi.org/10.1016/j.marchem.2017.06.006, 2017.

Smale, D. A., Wernberg, T., Oliver, E. C., Thomsen, M., Harvey, B. P., Straub, S. C., ... and Moore, P. J.: Marine heatwaves threaten global biodiversity and the provision of ecosystem services, Nat. Clim. Change, 9, 306–312, https://doi.org/10.1038/s41558-019-0364-4, 2019.

Solé, J., Ballabrera-Poy, J., Macías, D., and Catalán, I. A.: The role of ocean velocity in chlorophyll variability. A modelling study in the Alboran Sea, Sci. Mar., 80, 249–256, https://doi.org/10.3989/scimar.04290.04A, 2016.

Speich, S., Madec, G., and Crépon, M.: A strait outflow circulation process study: The case of the Alboran Sea, J. Phys. Oceanogr., 26, 320–340, https://doi.org/10.1175/1520-0485(1996)026<0320>2.0.CO;2, 1996.

Stanichny, S., Tigny, V., Stanichnaya, R., and Djenidi, S.: Wind driven upwelling along the African coast of the Strait of Gibraltar, Geophys. Res. Lett., 32, 1–4, https://doi.org/10.1029/2004GL021760, 2005.

Steinhoff, T. and Skjelvan, I.: Uncertainty analysis for calculations of the marine carbonate system for ICOS-Oceans stations, ICOS OTC, https://doi.org/10.18160/VB7C-Z758, 2020.

Taillandier, V., D'Ortenzio, F., and Antoine, D.: Carbon fluxes in the mixed layer of the Mediterranean Sea in the 1980s and the 2000s, Deep-Sea Res. Part I Oceanogr. Res. Pap., 65, 73–84, https://doi.org/10.1016/j.dsr.2012.03.004, 2012.

Takahashi, T.: Global air-sea flux of CO2 based on surface ocean pCO2, and seasonal biological and temperature effects, Deep-Sea Res. Part II, 49, 1601–1622, 2002.

Takahashi, T., Olafsson, J., Goddard, J. G., Chipman, D. W., and Sutherland, S. C.: Seasonal variation of CO2 and nutrients in the high-latitude surface oceans: A comparative study, Global Biogeochem. Cycles, 7, 843–878, https://doi.org/10.1029/93GB02263, 1993.

Takahashi, T., Sutherland, S. C., Chipman, D. W., Goddard, J. G., Ho, C., Newberger, T., and Munro, D. R.: Climatological distributions of pH, pCO_2, total CO_2, alkalinity, and CaCO3 saturation in the global surface ocean, and temporal changes at selected locations, Mar. Chem., 164, 95–125, https://doi.org/10.1016/j.marchem.2014.06.004. 2014.

Takahashi, T., Sutherland, S. C., Sweeney, C., Poisson, A., Metzl, N., Tilbrook, B., Bates, N., Wanninkhof, R., Feely, R. A., Sabine, C., Olafsson, J., and Nojiri, Y.: Global sea-air CO2 flux based on climatological surface ocean pCO2, and seasonal biological and temperature effects, Deep-Sea Res. Part II Top. Stud. Oceanogr., 49, 1601–1622, https://doi.org/10.1016/S0967-0645(02)00003-6, 2002.

Tanhua, T., Hainbucher, D., Schroeder, K., Cardin, V., Álvarez, M., and Civitarese, G.: The Mediterranean Sea system: A review and an introduction to the special issue, Ocean Sci., 9, 789–803, https://doi.org/10.5194/OS-9-789-2013, 2013.

Touratier, F., and Goyet, C.: Decadal evolution of anthropogenic CO2 in the northwestern Mediterranean Sea from the mid-1990s to the mid-2000s, Deep-Sea Res. Part I Oceanogr. Res. Pap., 56, 1708–1716, https://doi.org/10.1016/J.DSR.2009.05.015, 2009.

Turi, G., Lachkar, Z., and Gruber, N.: Spatiotemporal variability and drivers of pCO2 and air-sea CO2 fluxes in the California Current System: An eddy-resolving modeling study, Biogeosciences, 11, 671–690, https://doi.org/10.5194/BG-11-671-2014, 2014.

Turi, G., Lachkar, Z., Gruber, N., and Münnich, M.: Climatic modulation of recent trends in ocean acidification in the California Current System, Environ. Res. Lett., 11, 014007, https://doi.org/10.1088/1748-9326/11/1/014007, 2016.

Ulses, C., Estournel, C., Marsaleix, P., Soetaert, K., Fourrier, M., Coppola, L., Lefèvre, D., Touratier, F., Goyet, C., Guglielmi, V., Kessouri, F., Testor, P., and Durrieu De Madron, X.: Seasonal dynamics and annual budget of dissolved inorganic carbon in the northwestern Mediterranean deep-convection region, Biogeosciences, 20, 4683–4710, https://doi.org/10.5194/bg-20-4683-2023, 2023.

Van Heuven, S., Pierrot, D., Rae, J. W. B., Lewis, E., and Wallace, D. W. R.: MATLAB Program Developed for CO2 System Calculations, ORNL/CDIAC-105b, Carbon Dioxide Information Analysis Center, Oak Ridge National Laboratory, U.S. Department of Energy, Oak Ridge, Tennessee, https://doi.org/10.3334/CDIAC/otg.CO2SYS_MATLAB_v1.1, 2011.

Vargas-Yáez, M., Plaza, F., García-Lafuente, J., Sarhan, T., Vargas, J. M., and Vélez-Belchi, P.: About the seasonal variability of the Alboran Sea circulation, J. Mar. Syst., 35, 229–248, https://doi.org/10.1016/S0924-7963(02)00128-8, 2002.

Viúdez, A., Pinot, J. M., and Haney, R. L.: On the upper layer circulation in the Alboran Sea, J. Geophys. Res. Ocean., 103, 21653–21666, https://doi.org/10.1029/98JC01082, 1998.

Wanninkhof, R.: Relationship between wind speed and gas exchange over the ocean revisited, Limnol. Oceanogr. Methods, 12, 351–362, https://doi.org/10.4319/lom.2014.12.351, 2014.

Wanninkhof, R., Doney, S. C., Peng, T.-H., Bullister, J. L., Lee, K., and Feely, R. A.: Comparison of methods to determine the anthropogenic CO2 invasion into the Atlantic Ocean, Tellus B, 51, 511–530, https://doi.org/10.3402/tellusb.v51i2.16335, 1999.

Wanninkhof, R., Pierrot, D., Sullivan, K., Mears, P., and Barbero, L.: Comparison of discrete and underway CO2 measurements: Inferences on the temperature dependence of the fugacity of CO2 in seawater, Mar. Chem., 247, 104178, https://doi.org/10.1016/j.marchem.2022.104178, 2022.

Weiss, R.: Carbon dioxide in water and seawater: the solubility of a non-ideal gas, Mar. Chem., 2(3), 203–215, https://doi.org/10.1016/0304-4203(74)90015-2. 1974.

Whitehead, J. A., and Miller, A. R.: Laboratory simulation of the gyre in the Alboran Sea, J. Geophys. Res. Ocean., 84, 3733–3742, https://doi.org/10.1029/jc084ic07p03733, 1979.

Wimart-Rousseau, C., Lajaunie-Salla, K., Marrec, P., Wagener, T., Raimbault, P., Lagadec, V., Lafont, M., Garcia, N., Diaz, F., Pinazo, C., Yohia, C., Garcia, F., Xueref-Remy, I., Blanc, P. E., Armengaud, A., and Lefèvre, D.: Temporal variability of the carbonate system and air-sea CO2 exchanges in a Mediterranean human-impacted coastal site, Estuar. Coast. Shelf Sci., 236, https://doi.org/10.1016/j.ecss.2020.106641, 2020.

Wimart-Rousseau, C., Wagener, T., Álvarez, M., Moutin, T., Fourrier, M., Coppola, L., Niclas-Chirurgien, L., Raimbault, P., D'Ortenzio, F., Durrieu de Madron, X., Taillandier, V., Dumas, F., Conan, P., Pujo-Pay, M., and Lefèvre, D.: Seasonal and Interannual Variability of the CO2 System in the Eastern Mediterranean Sea: A Case Study in the North Western Levantine Basin, Front. Mar. Sci., 8, 1–18, https://doi.org/10.3389/fmars.2021.649246, 2021.

Wimart-Rousseau, C., Wagener, T., Bosse, A., Raimbault, P., Coppola, L., Fourrier, M., Ulses, C., and Lefèvre, D.: Assessing seasonal and interannual changes in carbonate chemistry across two time-series sites in the North Western Mediterranean Sea, Front. Mar. Sci., 10, https://doi.org/10.3389/fmars.2023.1281003, 2023.

Wolf-Gladrow, D. A., Zeebe, R. E., Klaas, C., Körtzinger, A., and Dickson, A. G.: Total alkalinity: The explicit conservative expression and its application to biogeochemical processes, Mar. Chem., 106(1–2), 287–300, https://doi.org/10.1016/j.marchem.2007.01.006. 2007.

Zambrano-Bigiarini, M., Majone, B., Bellin, A., Bovolo, C. I., Blenkinsop, S., and Fowler, H. J.: Hydrological impacts of climate change on the Ebro River basin, in: The Ebro River Basin, The Handbook of Environmental Chemistry, Springer, Berlin, Heidelberg. 13, 47–75, https://doi.org/10.1007/698_2010_85. 2010.

Zarghamipour, M., Malakooti, H., and Bordbar, M. H.: Air–Sea CO2 Exchange Over the Mediterranean Sea, the Red Sea and the Arabian Sea, Int. J. Environ. Res., 18, https://doi.org/10.1007/s41742-024-00586-6, 2024.